

Analysis of arc welding process in space

Dmitry G. Luchinsky SGT Inc., Ames Research Center, Moffett Field, California

Vasyl Hafiychuk SGT Inc., Ames Research Center, Moffett Field, California

Kevin R. Wheeler Ames Research Center, Moffett Field, California

Christopher E. Roberts Marshal Space Flight Center, Huntsville, Alabama

Ian M. Hanson Marshal Space Flight Center, Huntsville, Alabama

NASA STI Program...in Profile

Since its founding, NASA has been dedicated to the advancement of aeronautics and space science. The NASA scientific and technical information (STI) program plays a key part in helping NASA maintain this important role.

The NASA STI Program operates under the auspices of the Agency Chief Information Officer. It collects, organizes, provides for archiving, and disseminates NASA's STI. The NASA STI Program provides access to the NASA Aeronautics and Space Database and its public interface, the NASA Technical Report Server, thus providing one of the largest collection of aeronautical and space science STI in the world. Results are published in both non-NASA channels and by NASA in the NASA STI Report Series, which includes the following report types:

- TECHNICAL PUBLICATION. Reports of completed research or a major significant phase of research that present the results of NASA programs and include extensive data or theoretical analysis. Includes compilations of significant scientific and technical data and information deemed to be of continuing reference value. NASA counterpart of peer-reviewed formal professional papers, but having less stringent limitations on manuscript length and extent of graphic presentations.
- TECHNICAL MEMORANDUM.
 Scientific and technical findings that are preliminary or of specialized interest, e.g., quick release reports, working papers, and bibliographies that contain minimal annotation. Does not contain extensive analysis.
- CONTRACTOR REPORT. Scientific and technical findings by NASA-sponsored contractors and grantees.

- CONFERENCE PUBLICATION.
 Collected papers from scientific and technical conferences, symposia, seminars, or other meetings sponsored or co-sponsored by NASA.
- SPECIAL PUBLICATION. Scientific, technical, or historical information from NASA programs, projects, and missions, often concerned with subjects having substantial public interest.
- TECHNICAL TRANSLATION. Englishlanguage translations of foreign scientific and technical material pertinent to NASA's mission.

Specialized services also include organizing and publishing research results, distributing specialized research announcements and feeds, providing information desk and personal search support, and enabling data exchange services.

For more information about the NASA STI Program, see the following:

- Access the NASA STI program home page at http://www.sti.nasa.gov
- E-mail your question to help@sti.nasa.gov
- Phone the NASA STI Information Desk at 757-864-9658
- Write to: NASA STI Information Desk Mail Stop 148 NASA Langley Research Center Hampton, VA 23681-2199

NASA/TM-20210022016



Analysis of arc welding process in space

Dmitry G. Luchinsky SGT Inc., Ames Research Center, Moffett Field, California

Vasyl Hafiychuk SGT Inc., Ames Research Center, Moffett Field, California

Kevin R. Wheeler Ames Research Center, Moffett Field, California

Christopher E. Roberts Marshal Space Flight Center, Huntsville, Alabama

Ian M. Hanson Marshal Space Flight Center, Huntsville, Alabama

National Aeronautics and Space Administration

Ames Research Center Moffett Field, California 94035-2199

| Acknowledgments |
|---|
| |
| |
| |
| |
| |
| The use of trademarks or names of manufacturers in this report is for accurate reporting and does not |
| constitute an offical endorsement, either expressed or implied, of such products or manufacturers by the National Aeronautics and Space Administration. |
| |
| |
| Available from: |
| NASA STI Program / Mail Stop 148 NASA Langley Research Center Hampton, VA 23681-2199 |

Fax: 757-864-6500

Abstract

This work is motivated by NASA plans to conduct welding experiments on the ISS. It is expected that deployment of welding and additive manufacturing technologies in the space environment has the potential to revolutionise how orbiting platforms are designed, manufactured, and assembled. However, the structure, composition and quality of a weld is extremely dependent on the environment and can be difficult to control in space. Shielding gases would also be tough to manage as gases behave differently in zero gravity and airless environments. Additional points of concern are related to the spatter and sparks dynamics in space. Therefore there is a need for a more basic understanding of welding processes by computational modelling. To provide such an insight we developed state of art models of the ARC torch, droplet detachment and transfer, and the melt pool build up using magnetohydrodynamics approximation and level set method for two-phase liquid metal/gas flow modelling. Two finite element models were built using 2D axisymmetric geometry in COMSOL Multiphysics[®]: (i) stationary model of the ARC torch and (ii) dynamical model of droplet detachment and transfer. Both models demonstrate reasonable agreement with earlier experimental observations and high sensitivity to the temperature dependence of the thermophysical parameters on the system materials. The models were used to provide physical insight into ARC welding in various environments and geometries. It was shown, in particular, that there is a significant probability of gas bubbles trapping in the meltpool and a possibility of unbounded wondering of sparks in the welding chamber in zero gravity. In addition, we estimated metal evaporation rate that may be hazardous in the confined environment of the ISS. These issues raise concern of quality of the weld and safety for ISS applications.

1 Introduction

Yesterday's vision of in-space construction, repair, and maintenance by welding will become tomorrow's reality [1]. This statement made nearly 30 years ago finds its confirmation today. In particular, NASA seeks a paradigm shift in the design and manufacturing of space architectures to enable sustainable, flexible missions through on-demand fabrication, repair, and recycling capabilities for critical systems, habitats, and mission logistics and maintenance. In this context deployment of welding and additive manufacturing technologies in the space environment has the potential to revolutionise how orbiting platforms are designed, manufactured, and assembled [2].

This work is motivated by the NASA plans to conduct welding experiments on ISS. And the main goal of this work is to provide modelling support and physics insight for these experiments.

Russian cosmonauts who crewed the Soviet Soyuz 6 mission to space in 1969, were the first to experiment with welding in space. Although Soyuz 6 demonstrated that multiple processes could work in space, the experiments also illustrated [3] the challenges that traditional welding processes face off-planet. The structure, composition and quality of a weld depend on the distribution of temperature in the weld pool and the distribution of molten materials as the weld is formed, which is difficult to control in space. Welding techniques that rely on cautiously balanced shielding gases would also be tough to manage as gases behave differently in zero gravity and airless environments. Additional points of concern are related to the spatter and sparks dynamics in space.

Therefore there is a need for a more basic understanding of welding processes by computational modelling. The current state of art in developing such an understanding is based on magnetohydrodynamics approximation and two-phase flow methods for modelling the liquid metal/gas flow. The earlier results (see e.g. [4–12] and references therein) demonstrate that using this approach it is possible to achieve reasonably accurate predictions of the torch temperature and droplet dynamics. Similar approach is used for the current studies with the focus on the development of 2D axisymmetric stationary and dynamical versions of the model.

The selected approach requires the knowledge of thermophysical properties of both gas and metals for the wide range of temperatures [13]. However, detailed information on such properties of metals is hard to obtain experimentally and most computational efforts to date have used constant values for selected thermophysical properties [13]. In the current studies we attempted to answer the question whether the temperature dependency of the physical properties have a significant influence on the behaviour of the ARC welding model.

The results of the development and simulations of the 2D axisymmetric model are presented in this report with the emphases on the effects of the thermophysical properties and on performance of the model in the zero-G environment. In what follows the model is discussed in Sec.2 with two main subsections describing model equations and solution of these equations using COMSOL with temperature dependent thermophysical properties. The application of the model to stationary and dynamical analysis of the ARC welding with steel wire is discussed in Sec. 3.

The welding model with ER5256 alloy wire is considered in Sec. 4. The analysis of the welding regimes as a function of various model parameters including pressure, gravity, and current variation is discussed in Sec. 5. Finally, the results are summarised and the future work is outlined in Conclusions in Sec. 6.

2 Modeling ARC WELDING in COMSOL

There is a choice of software that can be used to build a multiphysics model observing several effects, such as plasma, two-phase flow, heat transfer, and electromagnetism. The suitable software packages include FLUENT [5], ANSYS [8], and COMSOL [12]. In this work we use COMSOL [14] because it offers a convenient and intuitive environment for multiphysics modelling and because successful application of this package to simulations of ARC welding was demonstrated in earlier work [11,12].

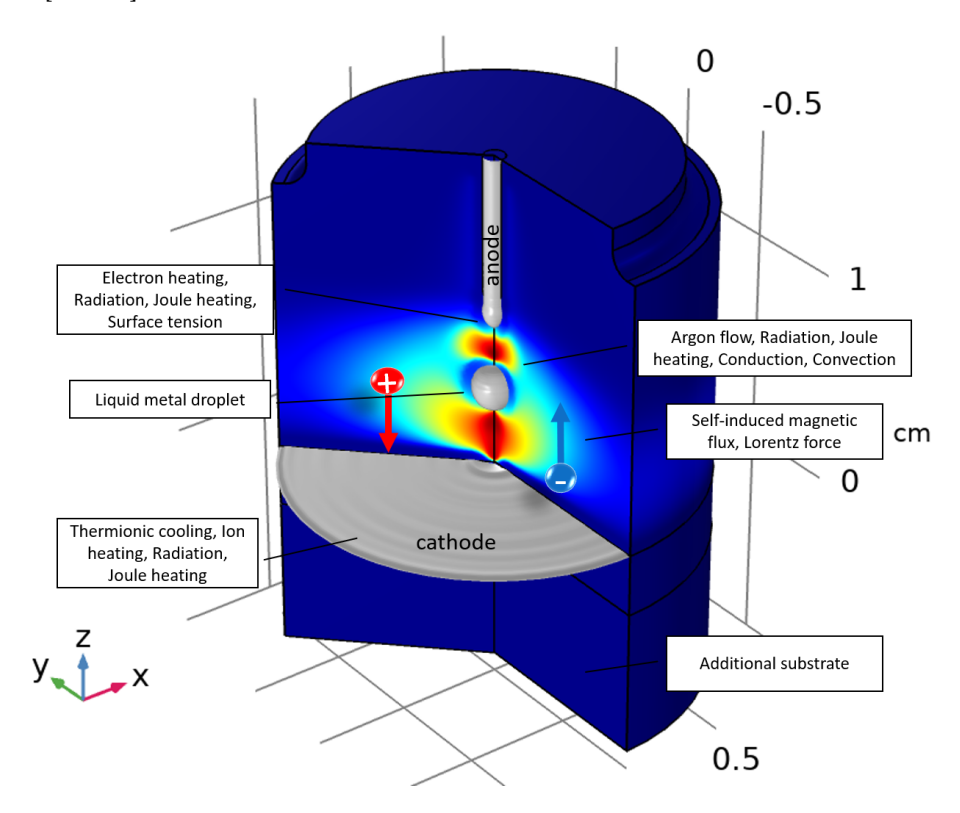


Figure 1. Schematics of the 2D axisymmetric COMSOL model with metal wire shown as anode and substrate surface shown as cathode. The liquid metal droplet approaching cathode surface after melting and separation from the wire tip is shown as a gray shiny ball in the center of the figure. The temperature profile developed in the ARC torch during droplet transfer is shown as coloured surface. Some of the major physical phenomena included into the model are listed in the boxes. The direction of the ion and electron flow are shown by the red and blue arrows respectively.

In the present report we restrict ourselves to the analysis of 2D axisymmetric model, in which plasma modelling is performed using magnetohydrodynamics ap-

proximation. The sketch of the model is shown in Fig. 1. The model captures the ARC torch dynamics developed in the Argon flow (with boundary conditions at the top pane and side surface of the figure), wire extrusion, droplet detachment, transfer to and impingement at the cathode surface. In addition, the model includes a number of important heat sources and forces. We will now consider the model equation in more details following mainly the work [12].

2.1 Model equations

In our development of the COMSOL model we follow mainly the work of Cadiou et all [12]. The adopted approach strongly correlates with other publications on the subject [5,8,15–17] and involves solution of the following sets of equations: (i) level set; (ii) conservation equations for mass, momentum and energy; (iii) equations for current conservation and magnetic vector potential. In addition, a number of forces and heat sources have to be introduced into the model to correct adopted approximations, including surface tension, buoyancy force, additional frictional and Darcy forces, thermionic emission at the substrate surface and electron heating of the metal wire, radiation in the bulk of the Argon flow, radiation at the metal surface and ion heating of the substrate surface, Joule heating of both metal and Argon flow. Because the model includes two fluids - liquid metal and argon gas - it should be considered within two-phase flow approximation. Also one has to take into account strong dependence of the material parameters on the temperature for both metal and argon gas, which makes model highly nonlinear and sensitive to the values of these parameters.

2.1.1 Level set

Following earlier work [12] we use the level set method [18] to describe the liquid-gas interface and simulate the electrode melting, detachment and transfer of droplets from the electrode tip to the substrate surface. Within this framework an additional variable ϕ (0 in the gas and 1 in the solid) is introduced into the system of equations. It defines the boundary between solid and gas phases and all the variables at the interface now have the form

$$\alpha = \alpha_{gas} + (\alpha_{metal} - \alpha_{gas})\phi \tag{1}$$

where α_{gas} represents the value of this variable in the gas phase and α_{metal} the corresponding value in the metal phase. ϕ satisfies the following equation

$$\frac{\partial \phi}{\partial t} + \mathbf{v} \cdot \nabla \phi = \gamma_{ls} \nabla \cdot \left(\varepsilon_{ls} \nabla \phi - \phi (1 - \phi) \frac{\nabla \phi}{|\nabla \phi|} \right)$$
 (2)

where **v** is the velocity, γ_{ls} is a reinitialization speed (m/s) and ε_{ls} is the interface thickness controlling parameter (m) that can be set up in COMSOL.

2.1.2 Conservation of mass and momentum

The fluid flow is modelled using laminar flow approximation. The conservation of mass is given by

$$\nabla \cdot \vec{v} = 0. \tag{3}$$

The momentum conservation is written as follows

$$\rho \left(\frac{\partial \vec{v}}{\partial t} + \nabla \vec{v} \cdot \vec{v} \right) = \nabla \cdot \left[-P\mathbf{I} + \mu_f \left(\nabla \vec{v} + (\nabla \vec{v})^t \right) \right] + \vec{F}_v$$
 (4)

where *P* is the pressure, **I** - the identity matrix, and μ_f - the dynamic viscosity. The volume force \vec{F}_v has the following components:

$$\vec{F}_{v} = \vec{F}_{mag} + \vec{F}_{gr} + \vec{F}_{ST} + \vec{F}_{Darcy} + \vec{F}_{fr}$$

$$\tag{5}$$

where \vec{F}_{mag} is the Lorentz force, \vec{F}_{gr} is the gravity force, \vec{F}_{ST} is the surface tension, \vec{F}_{Darcy} and \vec{F}_{fr} are additional Darcy and frictional forces respectively that will be discussed in more details below.

2.1.3 Conservation of energy

The heat transfer in the system is modelled using equation for the energy conservation

$$\rho C_p^{eq} \left(\frac{\partial T}{\partial t} + \vec{v} \cdot \nabla T \right) = \nabla \cdot (k \nabla T) + S_v$$
 (6)

where ρ is the density, C_p^{eq} is an equivalent specific heat, that equals C_p in the arcplasma domain, and is modified to $C_p + L_f \frac{df_L}{dT}$ in the metal domain to account for the latent heat of fusion L_f , k is the thermal conductivity, T is the temperature, f_L is the liquid fraction function given below in eq. (11), and S_v is a volumetric heat source term:

$$S_{v} = S_{IE} + S_{rad} + S_{CPI} + S_{API} + S_{LS} \tag{7}$$

where terms on the *rhs* are due to Joule effect, radiation, cathode/plasma interface, anode/plasma interface, and level set.

Joule effect. (bulk losses) Joule heating in the region of Ar flow and metal has the following form

$$S_{JE} = \vec{j} \cdot \vec{E}$$
 $\vec{j} = \sigma_e \vec{E}$ $\vec{E} = -\nabla V - \frac{\partial \vec{A}}{\partial t}$

Radiation. (bulk losses) Radiation from the bulk of Ar flow has the form

$$S_{rad} = -4\pi\varepsilon_N$$

where ε_N is the net emission coefficient of Argon taken from [5].

The heat sources applied at the metal/gas boundaries - cathode/plasma interface S_{CPI} , anode/plasma interface S_{API} , and level set S_{LS} - are discussed in the Sec. 2.1.6.

2.1.4 Electromagnetism

Magnetohydrodynamics model is completed [18] by including Maxwell's equations in the form

$$\nabla \cdot \left(\sigma_e \nabla V + \sigma_e \frac{\partial \vec{A}}{\partial t} \right) = 0 \tag{8}$$

$$\sigma_e \frac{\partial \vec{A}}{\partial t} + \frac{1}{\mu_0} \nabla \times (\nabla \times \vec{A}) + \sigma_e \nabla V = 0$$
(9)

where σ_e is the electrical conductivity, V is the electrical potential, μ_0 is the magnetic permeability and \vec{A} is the magnetic vector potential.

2.1.5 Forces

Electromagnetic force.

$$\vec{F}_{mag} = \vec{j} \times \vec{B} \left(1 + \frac{I_{max}}{I_{ave}} f_{curr} \right)$$
 (10)

where \vec{B} is the magnetic flux density and \vec{j} is the current density, f_{curr} is a periodic time function equal to 1 when the maximum current is applied and equal to 0 when the low current is applied. The latter term is introduced to stimulate the detachment of the droplet during the current pulse.

Darcy force. To approximate flow in the mushy zone we use additional Darcy force

$$\vec{F}_{Darcy} = -C \frac{1 - f_L^2}{f_L^3 + b} \vec{v}; \qquad f_L = \begin{cases} 1 & \text{if } T > T_L, \\ \frac{T - T_S}{T_L - T_S} & \text{if } T_S \le T \le T_L, \\ 0 & \text{if } T < T_S \end{cases}$$
(11)

where C is a large constant while b is a small constant and f_L is the liquid fraction function introduced above.

Artificial frictional force. At the wire plasma interface where $T > T_{melt}$

$$\vec{F}_{fric} = \left(F_{fric} \times \delta(\phi) \times f_{curr} \right) \vec{e}_z \tag{12}$$

where f_{curr} is the same as above and the interface "delta" function $\delta(\phi)$ is defined below.

Surface tension. Surface tension in COMSOL is included in the form

$$F_{st} = \left(\vec{n} \kappa + \left(I - \vec{n} \cdot \vec{n}^T \right) \nabla \gamma \right) \delta(\phi)$$

where κ is the curvature, γ is the surface tension coefficient, and $\delta(\phi)$ is the delta function approximation corresponding to the location of the metal/gas interface

$$\delta(\phi) = 6|\nabla \phi||\phi(1-\phi)|.$$

In general, surface tension is dependent on temperature and the common trend is that surface tension decreases with the increase of temperature, reaching a value of 0 at the critical temperature. Here we adopt a reduced form of the Buttler's equation [19]

$$\gamma = K_1 - K_2(T - T_C) + \dots, \tag{13}$$

where K_1 and K_2 are constants and T_C is the critical temperature. For example for steel 430 the values of these parameters are [19]: $K_1 = 1.8847$ N/m, $K_2 = 4.268 \times 10^{-4}$ N/m/K and $T_C = 1774$ K. Above critical temperature the surface tension is assumed constant. Unlike in many earlier publications [7,12,20] we allow surface tension to vary as a function of temperature. We find that the surface tension variation is a sensitive parameter of the model.

Buoyancy force In the ARC column, the volumetric forces are the sum of Lorentz F_{mag} eq. (10) and gravity forces

$$F_g = \rho(T)\vec{g}$$

whereas in the weld pool the buoyancy force is added in the form of Boussinesq approximation:

$$F_{g} = \rho_{0} \left(1 + w_{p} \beta (T - T_{ref}) \right) \vec{g} \tag{14}$$

where w_p is a variable that equals 1 in the weld pool and 0 elsewhere, ρ is the density, β is the coefficient of thermal expansion, \vec{g} is the gravity and T_{ref} is a reference temperature taken as the solidus temperature of the alloy.

2.1.6 Boundary heat sources

Balance of the heat sources plays one of the main roles in controlling welding regimes. Besides the Joule effect and radiation in the bulk Argon flow mentioned above, see Sec. 2.1.3, there is a very delicate balance of the sources and stinks of heat at the cathode/plasma and anode plasma interfaces, which we now consider in more details.

Cathode(substrate)/plasma interface. Radiation and convection losses are applied to the surface of the substrate. Convection losses are

$$q_c = -h_c(T - T_{am}),$$

where h_c is a convective heat transfer coefficient and T_{am} is ambient temperature. Radiation losses are

$$q_r = -\varepsilon \sigma_B (T^4 - T_{am}^4), \tag{15}$$

where ε is the metal emissivity, $\sigma_B = 5.67037441 \times 10^{-8} \ W \cdot m^{-2} \cdot K^{-4}$ is the Stefan-Boltzmann constant and T is the temperature at the metal surface.

In addition, substrate surface is heated by the ion current $j_i V_i$ and cooled by electron emission $j_e \phi_c$.

$$S_{CPI} = (j_i V_i - j_e \phi_c) \delta(\phi),$$

The term $j_i V_i$, represents the ionisation energy, where j_i is the ion current density and V_i the ionisation potential of the gas, j_e is the electron current density at the

surface of the cathode and ϕ_c the work function of the electrode. The current density j_e cannot exceed the Richardson-Dushmann density determined by equation:

$$j_{em} = A_r T^2 \exp\left(-\frac{e\phi_e}{k_B T}\right) \tag{16}$$

where A_r is the Richardson's constant, T is the temperature, e is the elementary charge, ϕ_e is the effective work function of the electrode and k_B is the Boltzmann constant. It is assumed that the ion current density j_i is the difference between normal component of the current density $j_c = |j.n|$ and Richardson-Dushmann density j_{em} at the cathode surface

$$j_i = \begin{cases} j_c - j_{em} & \text{if } j_c > j_{em}, \\ 0 & \text{if not} \end{cases}$$
 (17)

Anode(wire)/plasma interface. At the surface of the wire, which represents the anode, the heating is induced by the absorption of electrons

$$S_{API} = \left(\left| \vec{j}_a \cdot \vec{n}_a \right| \phi_a \right) \delta(\phi),$$

where ϕ_a is the anode work function and j_a the current density at the surface of the anode. The heat losses are due to radiation given by eq. (15) and possibly due to evaporation. Additional heat source has to be included at the anode/plasma interface. It is related to the fact that the sheath layer is not explicitly accounted by the model equations.

Level set. Following the discussion in the work [12] we introduce compensation of the shortcoming of the level set method related to the fact that within this method the conduction and radiation heat transfer at the anode plasma interface are strongly underestimated. The idea of [12] was to apply a Gaussian surface function to the end of the wire, whose power is the integral of the volume heat source calculated by the model in the form

$$S_{ls} = \begin{cases} (az+b)\frac{e^{-r^2/r_0^2}}{\pi r_0^2} \int_V S_{JE} dV \delta(\phi) & \text{at the wire/plasma interface,} \\ \frac{e^{-r^2/r_0^2}}{\pi r_0^2} \int_V S_{JE} dV \delta(\phi) & \text{at the substrate/plasma interface} \end{cases}$$
(18)

where Gaussian distribution parameter r_0 is taken equal to the radius of the electrode wire, while function (az + b) makes it possible to regulate the arc length in order to avoid short circuits. This correction facilitates the droplet detachment from the electrode tip.

To speed up the calculations we often approximate the integral using maximum value of the volumetric density loss (S_{JE}) in the ARC due to Joule effect as $\approx K \max(S_{JE})$, where K is a fitting parameter. Another important difference with earlier work [12] is that we apply this correction only at the wire tip/plasma interface.

2.2 Evaporation.

To estimate evaporation we follow the approach discussed in [21]. This approach relies on the assumption that there exists a thin layer of vapour near a liquid or solid is known as the Knudsen layer. The gas behaviour in this layer is locally not in equilibrium. The thickness of this layer is

$$l_K = \frac{k_B T_s}{\pi d^2 p_s}$$

where k_B is Boltzmann's constant, T_s is the temperature, p_s is the pressure, and d is the molecular diameter.

Following work [22] we only consider impact of the Knudsen layer on the evaporation rates and disregard fluid dynamics of the metal vapour. The metal evaporation can be described [23] by the flux of particles leaving (j^+) and returning (j^-) to the surface per unit time

$$j^{net} = j^{+} - j^{-} = \frac{\alpha N_A(p_s - p)}{\sqrt{2\pi MRT}}$$
 (19)

where α is the coefficient of evaporation (0 < α < 1), N_A is the Avogadro number, M is the molecular weight, R is the universal gas constant, and T is the absolute temperature at the evaporating surface. p_s is the standard vapour pressure of the substance, which is a function of the absolute temperature

$$\log p_s = \frac{A}{T} + B \log T + CT + D. \tag{20}$$

Here, A, B, C, and D are material constants.

For example for aluminium alloy the relation between pressure and temperature has the form [24,25] for solid

$$\log(p_s/Pa) = 14.465 - \frac{17342}{T/K} - 0.7927\log(T/K)$$
 (21)

and for liquid

$$\log(p_s/Pa) = 10.917 - \frac{16211}{T/K}.$$
 (22)

Similarly, for solid iron

$$\log(p_s/Pa) = 12.106 - \frac{21723}{T/K} + 0.4536\log(T/K)$$
 (23)

and for liquid iron

$$\log(p_s/Pa) = 11.353 - \frac{19574}{T/K}.$$
 (24)

We note that approximations for liquid metal are valid from the melting to boiling point given in Table 1. We further note that the maximum fluxes are obtained for the boiling points of both metals assuming $\alpha = 1$ and $p_h = 0$ in eq. (19). Then for the molecular flux we have

$$\Phi_e = 3.513 \times 10^{22} \frac{p_v}{\sqrt{MT}} \quad \left[\frac{molecules}{\text{cm}^2 s} \right]$$
 (25)

Table 1. Melting and boiling points of Al and Fe.

| Fe | [C] | [K] | Al | [C] | [K] |
|----------------------|------|---------|----|------|--------|
| Melting point | 1538 | 1811.15 | _ | 660 | 933.15 |
| Boiling point | 2861 | 3134.15 | _ | 2467 | 2740.2 |

and for the mass flux

$$\Gamma_e = 5.84 \times 10^{-2} \sqrt{\frac{M}{T}} p_v \quad \left[\frac{gr}{\text{cm}^2 s} \right]. \tag{26}$$

The corresponding heat flux due to evaporation is

$$q_{ev} = \Gamma_e \Delta H_{ev}$$

where heat of evaporation for steel and Al is given [26]

$$\Delta H_{ev}^{Al} = 11.4 \times 10^6 \quad \left[\frac{J}{\text{kg}}\right] \qquad \Delta H_{ev}^{st} = 7.34 \times 10^6 \quad \left[\frac{J}{\text{kg}}\right].$$

2.3 Modelling approach.

Equations with heat sources, boundary conditions, and additional forces (2)-(27) are solved numerically in COMSOL Multiphysics® [14] using finite element method (FEM). The following modules are used in simulations everywhere except additional substrate, see Fig. 1: Two-phase flow; Heat transfer; Electric currents; Magnetic fields. The simulations include multi-physics interfaces: Two-phase flow and Level set; and Nonisothermal flow. In the additional substrate only equations for thermal conductivity are solved.

Model assumptions. The commonly used assumptions [7, 12, 15, 27] of the 2D axisymmetric model are listed below:

- The model is solved in 2D axisymmetric, since the torch is static.
- The plasma is in local thermodynamic equilibrium (LTE). This assumption means that species such as ions and neutrons are supposed to have the same temperature.
- The fluid flow in the plasma and melt pool are considered to be Newtonian laminar and incompressible.
- Thermal dependence of the surface tension coefficient known as Marangoni effect is neglected because of the dispersion of values in literature (dependence of the exact chemical composition). Moreover, the Marangoni effect is believed not to be the predominant driven force here, since the falling of the numerous droplets in the melt pool causes a strong fluid flow.
- Buoyancy force is taken into account using the Boussinesq approximation.
- The effect of metal vapours on the mass flow coming from the vaporisation at the melt pool surface is not included in the model.

Floating potential. To impose constant current boundary condition at the wire inlet in COMSOL Multiphysics® we use floating potential boundary condition as suggested in [12].

Inlet boundary conditions for Ar velocity. The velocity at the Argon boundary conditions is set as fully developed flow with average velocity V_{in} at the inlet. The resulting velocity distribution should be compared to the analytical function [12]

$$v_{arg} = \frac{2Q_m}{\pi \rho} \frac{\left[R_{noz}^2 - r^2 + (R_{noz}^2 - R_w^2) \left(\frac{\ln(r/R_{noz})}{\ln(R_{noz}/R_w)} \right) \right]}{\left[R_{noz}^4 - R_w^4 + \frac{(R_{noz}^2 - R_w^2)}{\ln(R_{noz}/R_w)} \right]}$$
(27)

Impingement of the droplet on the substrate. The following picture of the droplet impingement is featured by this model. As discussed in [4] due to the competition among gravity, surface tension, electromagnetic, and arc drag forces, the droplet is elongated and a neck is formed before detachment. Then, the detached droplet is accelerated in the arc plasma by the combined effects of gravity, surface tension and the arc drag force. After the droplet hits the substrate surface, it quickly spreads out on the substrate surface.

The electrical current leaves the wire and droplet and enters the cathode through the arc space. The current density reaches its greatest value at the neck of the droplet.

Heat flux at the substrate surface. Heat flux at the cathode/substrate interface has three components: (i) cooling due to electron emission $(-|j_e|\phi_c\delta(\phi))$, where electron current density j_e does not exceed Richardson-Dushmann density, see eq. (16); (ii) cooling due to radiation emission, cf eq. (15) $Q_r = q_r\delta(\phi)$; (iii) heating due to ions impinging on the substrate $Q_i = j_i V_i \delta(\phi)$, see eq. (17).

We note that COMSOL does not allow to apply these boundary conditions at the moving boundary in level set two-phase flow model. To mitigate this issue we use normalised phase boundary delta function in the form

$$\delta(\phi) \rightarrow ls.delta/maxop1(ls.delta).$$

We emphasise that COMSOL does not currently support such an approach and developed model is in the grey zone. However, at present this is the only approach that allows to setup meaningful boundary conditions [12]. The obtained results have to be carefully verified and validated in the future work.

Heat flux at the anode interface Heat flux at the anode(wire)/plasma interface has the following components: (i) heating due to electron emission ($|j_e|\phi_c\delta(\phi)$); (ii) cooling due to radiation emission as above; (iii) additional heat source at the wire tip that compensates for the shortcomings of the level set method discussed in 2.1.6. In this case the heat source is applied only to the surface facing the substrate

$$\delta(\phi)_{+} \rightarrow ls.delta/maxop1(ls.delta) \cdot (dtang(phils, z) > 0).$$

We note that we have also experimented with the model by applying additional heat losses due to evaporation at the wire tip, droplet and melt pool surfaces.

Additional frictional force is applied at the metal/gas interface at the wire tip facing the substrate using $\delta(\phi)_+$ defined above.

Other boundary conditions were set according to the earlier work [12].

2.4 Temperature dependent parameters of argon

Thermophysical properties of Ar are well established in a wide range of temperatures. Earlier numerical work relies on this data, see e.g. [9]. We also use temperature dependent thermophysical properties of Ar in the form [28, 29] shown in Fig. 2. To verify the importance of these parameters we have studied dependence of the ARC torch on the temperature dependent parameters versus their constant values. It was shown that the ARC torch is sensitive to temperature dependence of all the parameters including viscosity, thermal conductivity, heat capacity, electrical conductivity, density, Richardson-Dushman current, density, and the net emission coefficient.

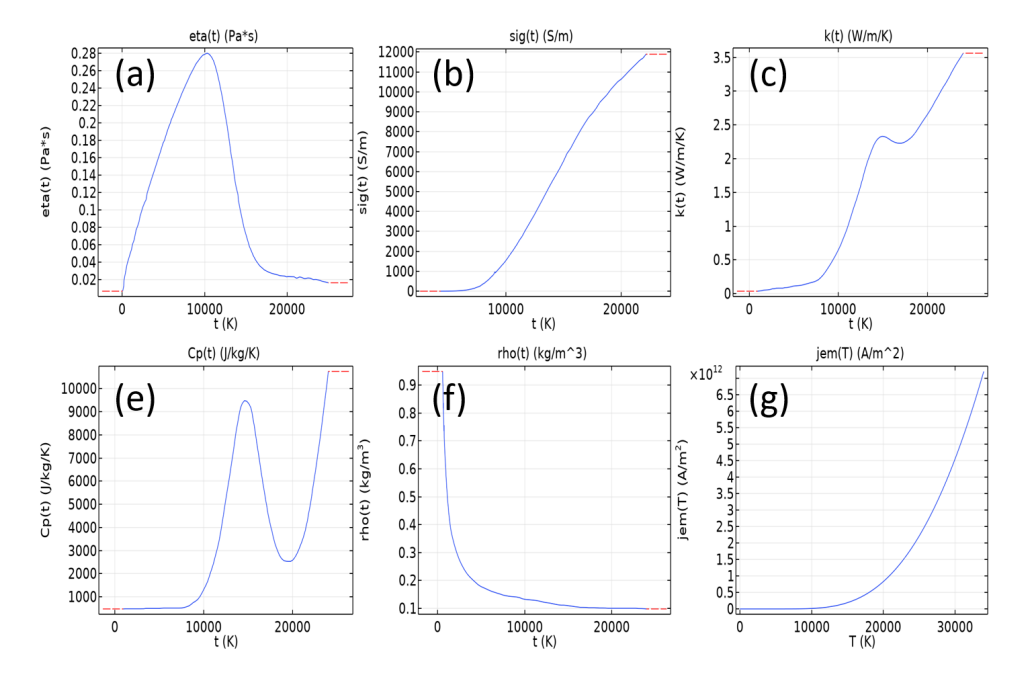


Figure 2. Temperature dependent parameters of argon: (a) viscosity; (b) electrical conductivity; (c) thermal conductivity; (d) specific heat capacity; (e) density; (f) Richardson-Dushman current, [9, 28, 29].

2.5 Thermophysical parameters of steel

Unlike in the case of Ar there remains uncertainties in the definition of thermophysical properties of steel for the wide range of temperatures required for the ARC modelling. The values used in our model are shown in Table 2 and Fig. 3. Some of the parameters are known only approximately and were used as fitting parameters bounded by literature data. The corresponding references in the table are indicated with asterisk. The approximation used to fit these parameters is explained below.

Table 2. Thermophysical parameters of steel. Symbol * indicate that these values were used fr estimations only

| Variable name | units | Stainless steel | Ref | Ar | Ref |
|---|--|--|-------|-----------------|----------|
| Thermal conductivity (k) | $(W.m^{-1}.K^{-1})$ | k(T) | [30] | k(T) | [28, 29] |
| Specific heat (C_p) | $(J.kg^{-1}.K^{-1})$ | $C_p(T)$ | [30] | $C_p(T)$ | [28, 29] |
| Density (ρ) | (kg.m ⁻³) | (ρ_s, ρ_f, ρ_l) | [31]* | $\rho(T)$ | [28, 29] |
| Dynamic viscosity (η) | (Pa.s) | (η_s, η_f, η_l) | [31]* | $\eta(T)$ | [28, 29] |
| Electrical conductivity (σ) | (S.m ⁻¹) | $(\sigma_s, \sigma_f, \sigma_l)$ | [32]* | $\sigma_e(T)$ | [33] |
| Magnetic permeability (μ_0) | (H.m ⁻¹ | 4 pi x 10 ⁻⁷ | [34] | - | - |
| Liquidus temperature (T_l) | (K) | 1723 | [35] | - | - |
| Solidus temperature (T_S) | (K) | 1673 | [35] | - | - |
| Melting temperature (T_{fus}) | (K) | 1700 | [35] | - | - |
| Net emission coefficient (ϵ_N) | (W.m ⁻³ .ster ⁻¹) | - | - | $\epsilon_N(T)$ | [5] |
| Surface tension coefficient (γ) | (N.m ⁻¹) | $(\gamma_s, \gamma_f, \gamma_l)$ | [5]* | - | - |
| Anode work function (ϕ_a) | (V) | 4.65 | [36] | - | - |
| Cathode work function (ϕ_c) | (V) | 4.65 | [36] | - | - |
| Effective work function (ϕ_e) | (V) | 2.63 | [36] | - | - |
| Richardson's constant (Ar) | $(A.m^{-2}.K^{-2})$ | 3×10^4 | [36] | - | - |
| Ionization potential (Vi) | (V) | 15.68 | [36] | - | - |
| Reinitialization speed (γ_{ls}) | (m/s) | $10 \cdot (T > T_{fus}) + 10^{-3} \cdot (T \le T_{fus})$ | - | - | |
| Interface thickness (ϵ_{ls}) | (µm) | 90 | - | - | - |

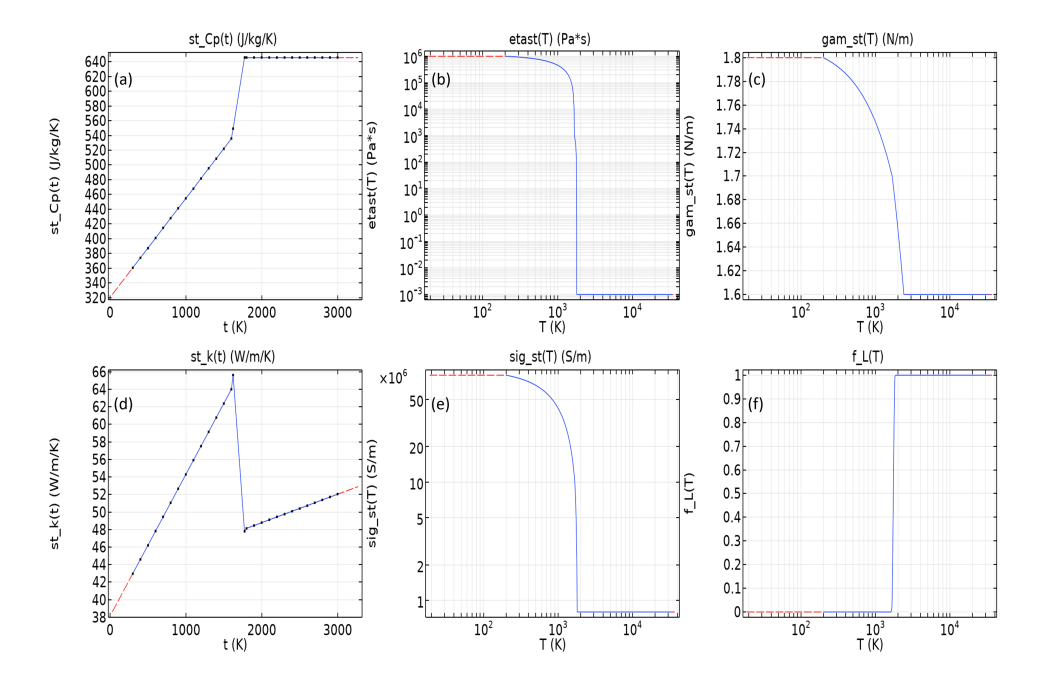


Figure 3. Temperature dependent parameters of steel: (a) specific heat capacity; (b) viscosity; (c) surface tension; (d) thermal conductivity; (e) electrical conductivity; (f) liquid fraction function of the temperature.

The triplets in lines 3-5, and 11 correspond to the approximation of the material parameters as shown in Table 3. Values of T_s and T_l are given in the Table 2

while $T_0 = 200K$ in our model. Examples of this approximation are shown in the Fig. 3 (b), (c), and (e).

Table 3. Approximation for some of the unknown temperature dependent parameters of metals

| $\overline{T_0}$ | \rightarrow T _s | $(X_s \cdot (T-T_0)/(T_s-T_0) + X_0 \cdot (T_s-T)/(T_s-T_0))$ |
|------------------|------------------------------|---|
| T_s | \rightarrow T _l | $(X_l \cdot (T-T_s)/(T_l-T_s) + X_s \cdot (T_l-T)/(T_l-T_s))$ |
| T_{l} | \rightarrow 34000 K | X_l |

3 Application to steel welding

There are generally three levels of the finite element modelling of the ARC welding. Firstly, stationary 2D model was developed and reported in the literature [17,36,37]. This model was mainly focused on the analysis of the temperature distribution in the ARC welding and validating the numerical results with experimental data. More recently, 2D-axisymmetric dynamical model has become available [10,12,15,38]. Corresponding modelling efforts were devoted to the development and validation of the dynamics of droplet detachment and transfer during welding. Currently, 3D dimensional modelling approach is under development [11,39,40] with the focus on the extending dynamical analysis to the welding pool. In this work we limit our research to the two initial steps: (i) stationary 2D-axisymmetric model; and (ii) dynamical 2D-axisymmetric model. The 3D modelling was only initially tested. It was shown that extension to the 3D model is very demanding in terms of computing power and computational time and should be developed at the next stage of the research.

Some results obtained using stationary and dynamical 2D-axisymmetric modelling approach will be considered below.

3.1 Stationary 2D-axisymmetric ARC torch model

In the stationary 2D-axisymmetric model, parameters of the steel were taken to be independent of the temperature as shown in the Table 4. All the Ar parameters were temperature dependent including density as was discussed in Sec. 2.4. In stationary case eq. (2) is not included into the model while eqs. (4) and (6) are considered to be time independent.

Table 4. Parameters of steel in stationary 2D axisymmetric model.

| Parameter name | Notation | Value | Units |
|---|--|---|------------------------------|
| Relative permeability | $\mu_{r,iso}$; $\mu_{r,ii} = \mu_{iso}$, $\mu_{r,ij} = 0$ | 1 | - |
| Electrical conductivity | σ_{iso} ; $\sigma_{ii} = \sigma_{iso}$, $\sigma_{ij} = 0$ | 4.032e8[S/m] | S/m |
| Coefficient of thermal expansion | α_{iso} ; $\alpha_{ii} = \alpha_{iso}$, $\alpha_{ij} = 0$ | 12.3e-6[1/K] | 1/K |
| Heat capacity at constant pressure Relative permittivity | Cp $\epsilon_{r,iso}$; $\epsilon_{r,ii} = \epsilon_{r,iso}$, $\epsilon_{r,ij} = 0$ | 475[J/(kg*K)] 50 | J/(kg·K) |
| Density Thermal conductivity | rho k_{iso} ; $k_{ii} = k_{iso}$, $k_{ij} = 0$ | 7850[kg/m3] 44.5[W/(m·K)] | kg/m ³ W/(m⋅K) |
| Ratio of specific heats Dynamic viscosity | gamma η | $ \begin{array}{c} 1 \\ \eta_{st}(T) \cdot (1-P) + \eta_{M} \cdot P \end{array} $ | - Pa·s |

The highly nonlinear dependence of the material parameters on the temperature caused a convergence problem. To overcome this issue we have employed nonlinearity ramping in COMSOL. According to this technique the nonlinear parameters of Ar were represented as weighted sums of the constant values corresponding to the ambient temperature and the temperature dependent value as shown in the Table 5. For example density of Ar in this approach is $1 \cdot P + (1 - P) \cdot \rho(T)$ in units kg/m^3 . The value of the parameter P is ramped in several steps:

$$[1.0:-0.05:0.1]$$

During ramping the magnetic field was excluded from the solution. It was added to the second (final) step of the solution.

Table 5. Parameters of Ar in stationary 2D axisymmetric model.

| Parameter name | Notation | Value | Units |
|------------------------------------|---|--------------------------------------|-------------------|
| Density | ρ | 1 · P+(1-P)·ρ(T) | kg/m ³ |
| Dynamic viscosity | η | $0.04 \cdot P + (1-P) \cdot \eta(T)$ | Pa·s |
| Thermal conductivity | $k_{i}so$; $k_{ii} = k_{iso}$, $k_{ii} = 0$ | 0.05· P+(1-P)· k(T) | W/(m·K) |
| Heat capacity at constant pressure | $C_{\mathcal{D}}$ | 1100· P+(1-P)· C _p (T) | J/(kg·K) |
| Ratio of specific heats | γ' | 1.4 | 1 |
| Electrical conductivity | σ_{iso} ; $\sigma_{ii} = \sigma_{iso}$, $\sigma_{ij} = 0$ | 5000⋅ P+(1-P)⋅ sig(T) | S/m |
| Relative permittivity | $\epsilon_{r,iso}$; $\epsilon_{r,ii} = \epsilon_{r,iso}$, $\epsilon_{r,ij} = 0$ | 5 | 1 |
| Relative permeability | $\mu_{r,iso}$; $\mu_{r,ii} = \mu_{r,iso}$, $\mu_{r,ij} = 0$ | 1 | 1 |

Stationary 2D model was validated by comparison with earlier numerical and experimental data, see Fig. 4. It can be seen from the figure that both the shape and the temperature in the ARC are in reasonable agreement with the experimental and earlier numerical data. The ARC in our model was obtained for wire radius 0.8 mm and tip was situated 7 mm above the substrate. The maximum temperature in the ARC is $\approx 17,000~\text{K}.$

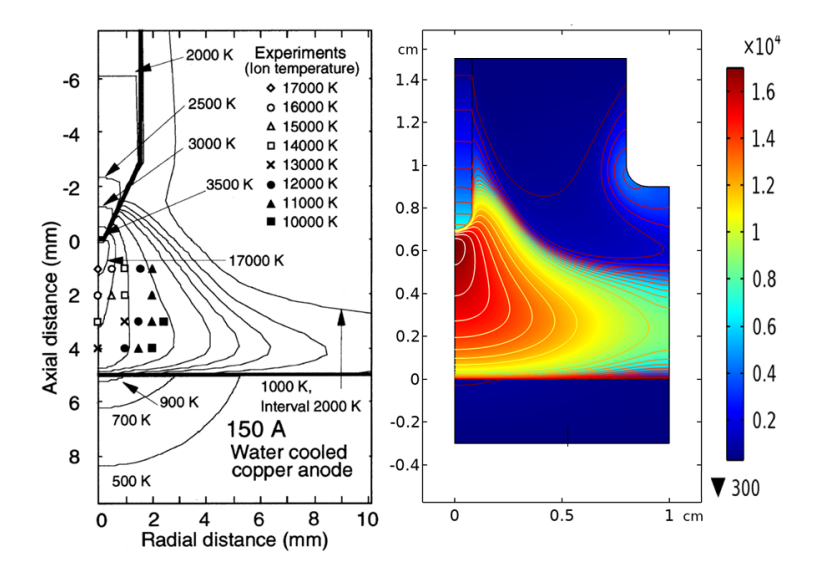


Figure 4. (left) Experimental and numerical data taken from [36], cf [6, 9, 37]. (right) Stationary solution for the temperature distribution in 2D-axisymmertic ARC torch model.

This model allows to analyse a wide range of physical variables and their dependencies on the parameters of the system. Examples of the model outputs are shown in Fig. 5.

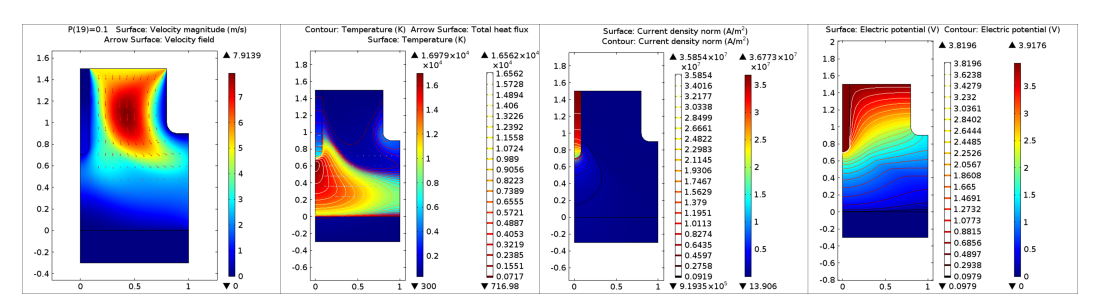


Figure 5. Example of the output variables of 2D-axisymmertric ARC torch model (left to right): (i) velocity; (ii) temperature; (iii) electric current density; (iv) electric potential.

To get insight into the physical effects of various parameters of the system we conducted extensive parametric studies of the model. An example of such studies is provided in Fig. 6, which shows dependence of the convective heat flux on the Ar inlet velocity. The analysis reveals a number of important features. Firstly, it is clear that the convective heat transfer plays a very important role in establishing temperature distribution in the ARC especially in the proximity of the wire tip.

Secondly, the studies reveal a strong dependence of the convective heat transfer on the velocity. Finally, it could be seen from the figure that there exist an optimal value of the inlet velocity $\approx 3~m/s$ for which the convective flux at the wire tip has maximum value. We note that this example of parameter dependence is typical and we conclude that the choice of the regime of welding requires careful optimisation that depends on the system environment.

We now consider extension of this model to the time-dependent analysis of the droplets detachment from the wire tip and their transfer to the substrate.

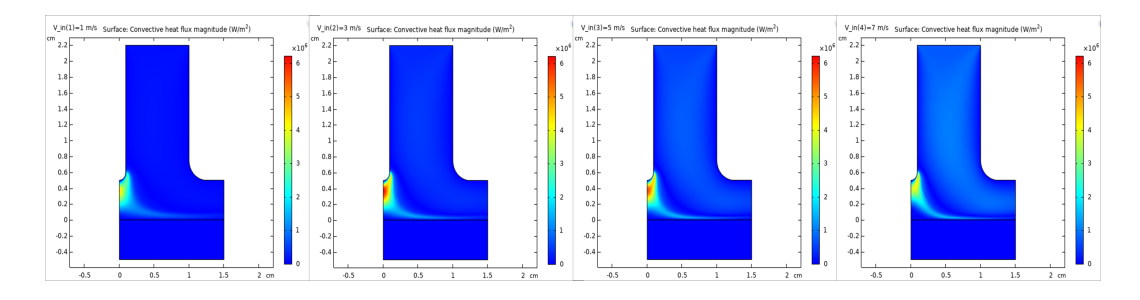


Figure 6. Dependence of the convective heat transfer flux on the following values of the inlet velocity (left to right): (i) 1 m/s; (ii) 3 m/s; (iii) 5 m/s; (iv) 7 m/s.

3.2 2D-axisymmetric model of droplet detachment and transfer

To model droplet detachment and transfer from the wire tip to the substrate the full time-dependent version of eqs. (2), (4), and (6) is considered. Furthermore, all the main material parameters of the steel are now considered to be temperature dependent as was discussed in the Sec. 2.5.

An example of the snapshot of the droplet transfer is shown in Fig. 7. The following steel parameters were used in these¹ simulations: (i) current - 170 A; (ii) interface thickness 75 $\mu(m)$; (iii) reinitialization parameter - 0.8; (iv) scaling parameter K of the heat transfer at the wire tip in eq. (27) - 6; (v) surface tension is given by Table 3 with (X_0, X_s, X_l) =(1.9;1.8;1.6) and T_l = 2400K; (vi) viscosity is given by the triplet (10⁶;1000;0.001) with T_l = 1723K; (vii) electrical conductivity triplet is (8×10⁷;1×10⁷;5×10⁶); and (viii) wife feed speed 10 cm/s.

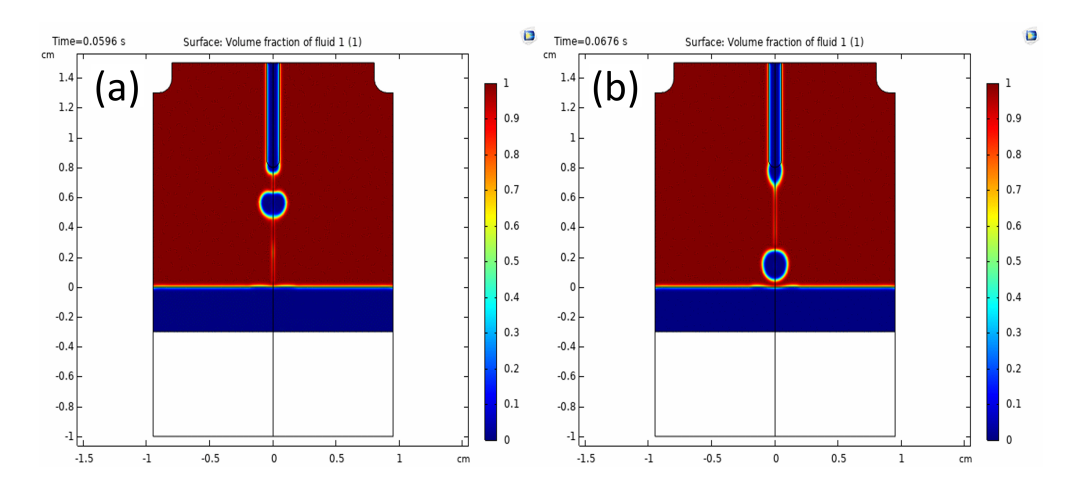


Figure 7. A snapshot of the droplet transfer at: (a) t=0.0596 s and (b) t=0.0676 s.

The following features can be seen from the figure. The droplet diameter is of the order but larger than the wire diameter. The time of the first droplet approaching the substrate is of the order 100 ms. The background is sufficiently clean. However, some leakage current from the wire to the substrate can be noticed. Importantly, the parameters of the problem listed above (droplet shape and size, droplet frequency, current and leakage current) are some of the key model parameters that require fitting using experimental data.

In addition, a very important characteristics of the ARC dynamics is the temperature distribution during droplet detachment and transfer. Examples of the temperature distribution for six snapshots are shown in Fig. 8 for the model². Parameters of simulations are very similar to the ones used for Fig. 7: (i) current - 200 A; (ii) interface thickness 75 $\mu(m)$; (iii) reinitialization parameter - 0.8; (iv) scaling parameter K of the heat transfer at the wire tip in eq. (27) - $Q_{int} = 1$; (v) sur-

¹\R56_L\TUNING\TUNNING\out_E_I170_d70_g08_Q6_ga19_16_et1e6_3_m3_B3e5_S8e7_7_6_kp0_F105_1e6

²\R56_L\TUNING\TUNNING_rec\out_E_I200rec_d70_g08_Q1_ga19_16_et1e6_3_m3_B3e5_ S8e7_2e7_8e6_kp0_F105_1e6_em

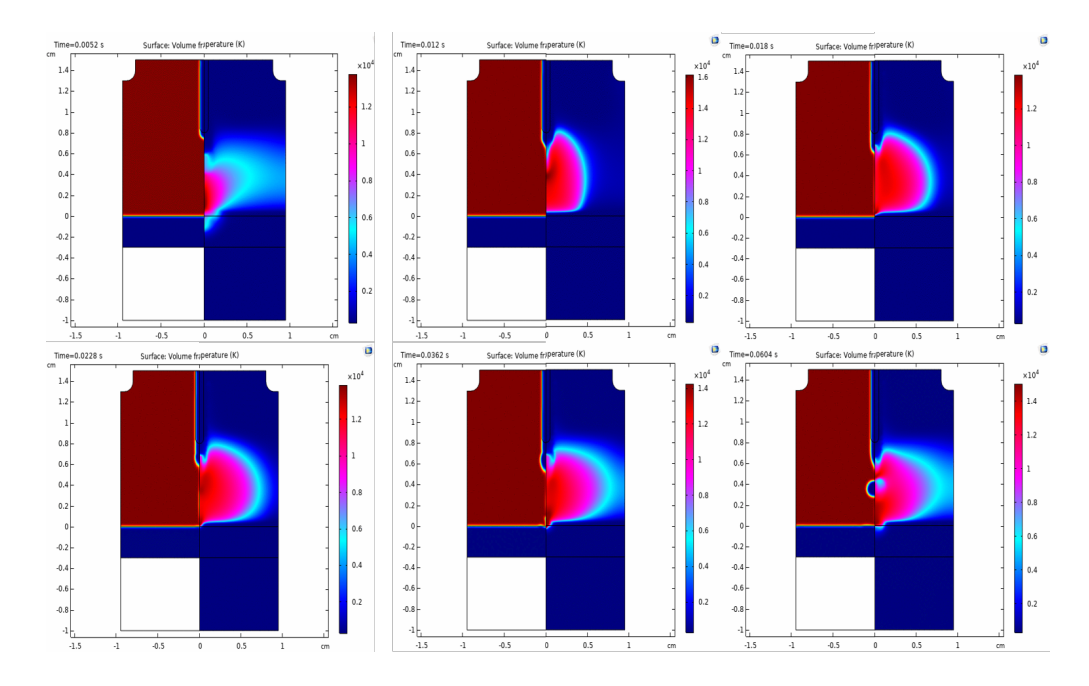


Figure 8. Time dependence of the volume fraction (left) and temperature (right) of steel (from the top left to the right bottom): 5.2 ms; 12 ms; 18 ms; 22.8 ms; 36.2 ms; and 60.4 ms.

face tension is given by Table 3 with (X_0, X_s, X_l) =(1.9;1.8;1.6) and T_l = 2400K; (vi) viscosity is given by the triplet (10⁶;1000;0.001) with T_l = 1723K; (vii) electrical conductivity - (8×10⁷;1×10⁷;5×10⁶); and (viii) wife feed speed 10 cm/s.

We note that in the case shown in the figure the current was applied using square pulses (from 0.01 to 0.08 s) with minimum current 20 A and maximum current 180 A.

It can be seen from the figure that the droplet heats up significantly above melting temperature during detachment. It is generally expected [41] that the droplet surface temperate may be of the order 3000 K, which is below the temperature observed in simulations. However, the simulations shown in the figure do not include evaporation.

Evaporation could in principle reduce droplet temperature following discussion in Sec. 2.2. However, in the present model we simply limit the droplet temperature by 3500 K.

The droplet dynamics is significantly affected by the forces acting on the droplet and it's neck during separation and transfer. In the Sec. 2.1.5 we discussed four such forces: (i) Lorentz force F_{mag} ; (ii) Darcy force F_{Darcy} ; (iii) surface tension F_{st} ; and (iv) additional frictional force F_{friq} . The action of the Lorentz force is illustrated in Fig. 9. The figure shows z-component of the force during droplet detachment. Three snapshots during time 0.0582 - 0.059 s illustrate the growth of the force at the neck of the droplet right before the detachment at time 0.0582 s. The volume force approaches 10^8 N/m^3 .

The surface tension force for the same detachment time (0.0582 s) is shown in

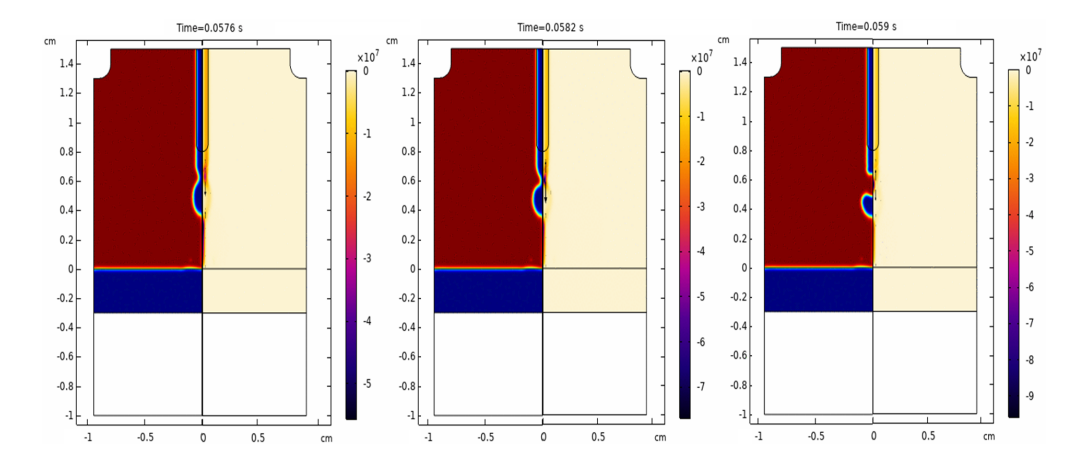


Figure 9. Time dependence of the volume fraction (left) and Lorentz force (right) of steel during droplet separation (from left to right): 57.6 ms; 58.2 ms; and 59 ms. The *z*-component of the Lorentz force is shown by vertical arrows at the droplet neck. Color bar shows the strength of the force.

Fig. 10 (left). The value of this force is close to the value of the Lorentz force but it is smaller and directed towards the axis at the droplet neck and the towards the centre of the droplet at the droplet surface. In the current simulation the Darcy force is a few orders of magnitude smaller as compared to the surface tension. The main purpose of the Darcy force is to control shape and dynamics of the melt pool by slowing down flow in the mash zone.

The additional frictional force is one order of magnitude smaller than surface tension force. The key function of the additional frictional force is to correct frequency of the droplet detachment in accordance with experimental observations.

We note that the Darcy force does not strongly correlate with other forces and can be tuned independently. Surface tension and additional friction forces on the other hand do counterpart each other at the surface of the droplet and wire tips. Surface tension tends to round the droplet while additional friction force is enforc-

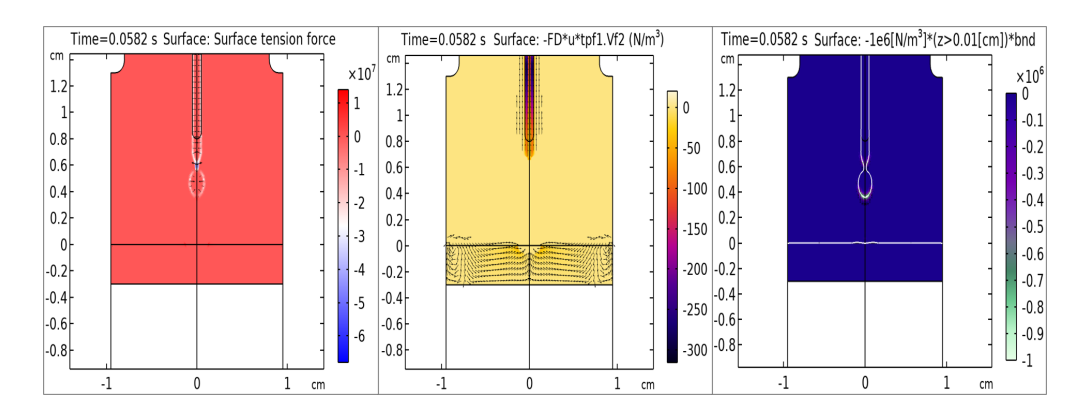


Figure 10. (left) Surface tension at time t = 0.0582 s. (middle) Darcy force for t = 0.0582 s. (right) Additional frictional force for t = 0.0582 s.

ing detachment of the droplet from the wire tip. Therefore the latter two forces have to be carefully balanced with each other and it is expected that surface tension should exceed additional frictional force as it has clear physical meaning. We note, that it is expected on the ground of experimental observations [42] that gravity force is an order of magnitude smaller as compared to the plasma force on the droplet, see also Sec. 5.4.

Overall, our studies demonstrate that 2d-axisymmetric dynamical model can reproduce the main experimentally observable features of ARC welding including droplet shape and frequency, shape and dynamics of the melt pool, shape and temperature distribution in the ARC, and electric current density.

We now consider an application of this modelling approach to the wire alloy ER5356.

4 Application to ER5356 welding

To adopt the developed approach for modelling ARC welding with ER5356 wire one has to change parameters of the metal.

4.1 Temperature dependent parameters of ER5356

Some information about parameters of ER5356 is collected in Table 6. Most of the parameters are constants. Some further insight into temperature dependence of these parameters can be gained by analysing results for similar alloys [43], but at present we do not have accurate experimental data for temperature dependent parameters of ER5356.

Table 6. Thermophysical parameters of ER5356.

| Parameters | Values SGC | Values SI Comments | |
|-----------------------|---|------------------------|--|
| Melting | 1060-1175[F] | 571-635 C 944-1008 K | |
| Surface ten- sion | | 1.2-0.8 N/m (?) | |
| Density | 0.096[lb/in3] | 2657.3 kg/m3 | |
| Conductivity | 29%IACS | 2x10 ⁷ S/m | |
| Thermal conductivity | https://www.azom.com/ article.aspx? ArticleID=6654 | 116 W/m/K | |
| Heat capaci- tance | https://www.ncbi. nlm.nih.gov/pmc/ articles/PMC7956743/ | 1000 J/kg/K | |
| Viscosity | | 105-0.01 Pa·s (?) | |

To speed up the development of the model within the current project we used estimations shown in the table and in work [43] and the results known for the steel. We have adjusted data used for the steel to be consistent with the corresponding known values for the alloy ER5356. Examples of the temperature dependent parameters of ER5356 alloy used in the model are shown in the Fig. 11. One of the main changes in the thermophysical parameters of the alloy ER5356 as compared to the steal is significantly reduced melting temperature. We also note that the

electrical conductivity, density, and surface tension in ER5356 are reduced as compared to steel while specific heat and thermal conductivity are higher for ER5356.

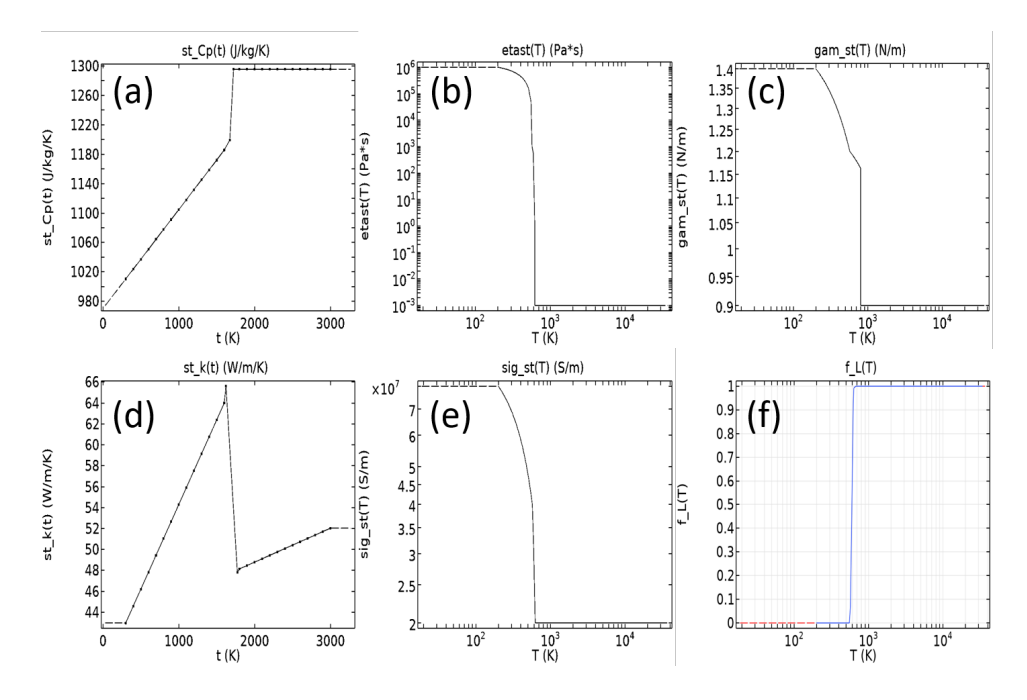


Figure 11. Temperature dependent parameters of the ARC welding with the alloy ER5356 wire: (a) specific heat capacity; (b) viscosity; (c) surface tension; (d) thermal conductivity; (e) electrical conductivity; (f) liquid fraction function of the temperature.

The results of the simulation of the ARC plasma with ER5356 wire are shown in Fig. 12, which should be compared to the Fig. 12. The temperature distributions for six snapshots are shown in Fig. 12 for the model³. Parameters of simulations are very similar to the ones used for Fig. 7: (i) current - 90 A; (ii) interface thickness 75 μ (m); (iii) reinitialization parameter - 0.8; (iv) scaling parameter K of the heat transfer at the wire tip in eq. (27) - Q_{int} = 1; (v) surface tension is given by Table 3 with (X_0, X_s, X_l) (1.4;1.2;0.9) and T_l = 800 K; (vi) viscosity is given by the triplet (10⁶;100;0.001) with T_l = 623 K; (vii) electrical conductivity - (8× 10⁷; 8× ⁶; 6× 10⁶); and (viii) wife feed speed 10 cm/s.

As expected qualitatively the results are very similar to those obtained for steel wire including the droplet shape and frequency. The main difference is that the peak values for the ARC and droplet temperature are lower than for the steel. Importantly, the ARC welding regime with droplet formation and transfer is obtained for much lower current ≈ 100 A as compared to ≈ 200 A for steel. The latter difference is in agreement with experimental observations.

We now apply developed 2D-axisymmetric dynamical model to estimate effects of various parameters on the welding regime.

³\R56_L\ER5356\tun_I\out_E5356_I90rcb_d70_g08_01_ga14_09_et1e6_2_0001_B3e5_S8e7_ 8e6_6e6_kp30_F105_1e6_Cp400_vin13

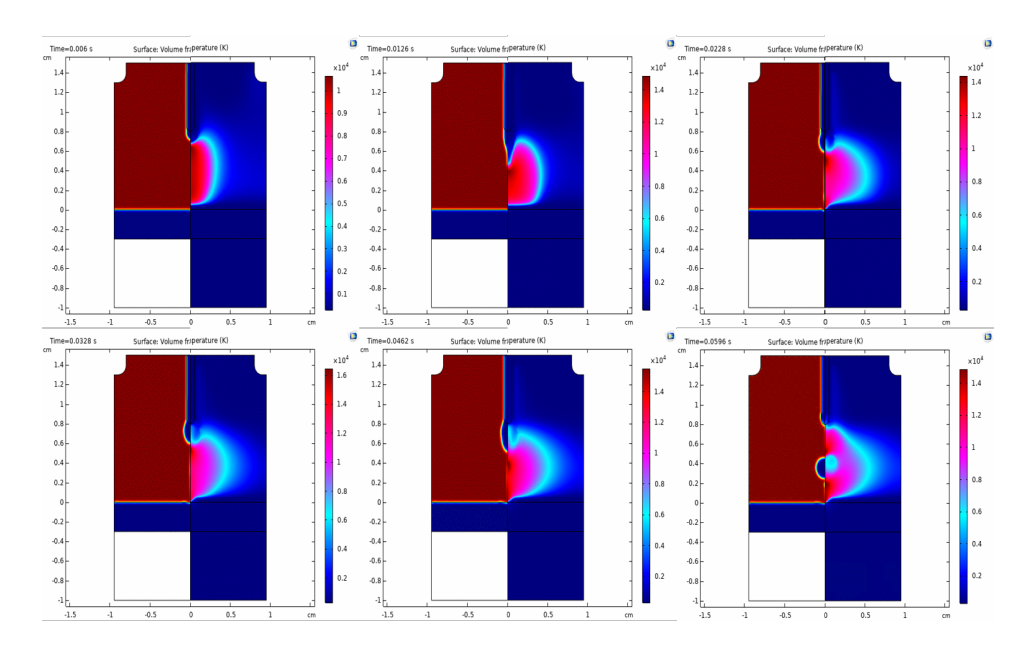


Figure 12. Time dependence of the volume fraction (left) and temperature (right) of ER5356 from top left to the right bottom: 0.6 ms; 12.6 ms; 22.8 ms; 32.8 ms; 42.6 ms; and 59.6 ms.

5 Parameter dependence of the welding regime

5.1 Sensitivity of the model with respect to parameters

One of the challenges of the developed approach is a large number of model parameters. A subset of the parameters used in simulations is shown in Fig. 13. One can immediately notice a large number of temperature dependent parameters for both gas and metal. We notice that many of these parameters in turn depend of a few sub-parameters, see Table 3. In addition, there is a large number of other important model parameters, see the middle column of the Fig. 13. Overall, there are more than 50 parameters that can be used to fit various welding regimes observed in experiments.

The problem of performing sensitivity analysis is related to the fact that dynamical model has to be solved for each value of the parameter and each solution takes a few hours. Furthermore, the system response to the changes of one parameter depend on values of all other parameters.

To address these issues we have performed extensive simulations of the model by varying one of the parameters. These results should be considered as preliminary because we had to perform simultaneous optimisation of the model and the results of the sensitivity analysis were obtained for slightly different welding regimes. On the ground of several hundred simulations we have developed intuition what parameters are most important for tuning the model to specific experimentally observed welding regimes.

According to the results of simulations of stationary model we concluded (see

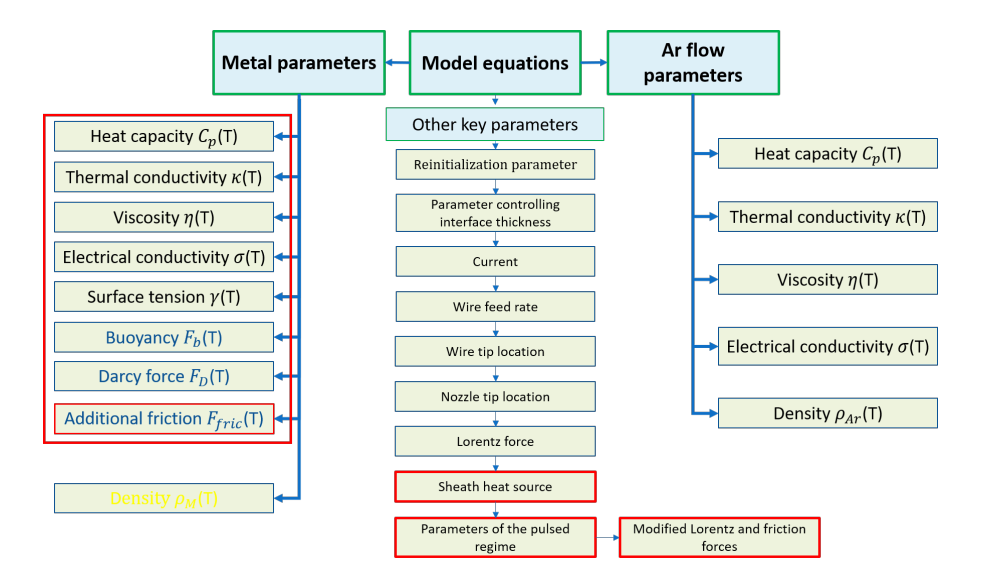


Figure 13. Some of the temperature dependent thermophysical parameters of the metal (left column) and gas (right column) used in the model. Additional important constant parameters are shown in the middle column.

Sec. 3.1) that it is important to keep all the temperature dependent thermophysical parameters of Ar in the model. Maximum temperature and the temperature distribution in the ARC torch are very sensitive to all these parameters. The system is especially sensitive with respect to viscosity $(\eta(T))$ and electrical conductivity $(\sigma(T))$.

Dynamical model is also very sensitive to the temperature dependent thermophysical parameters of both Ar and metal. Specifically, the model is very sensitive with respect to electrical conductivity $(\sigma(T))$, surface tension $(\gamma(T))$, and viscosity $(\eta(T))$ of the metal. Below we consider in more details response of the model to some of the parameters.

5.2 Effect of the current

Typical current dependence is shown in Fig. 14. In this figure the volume fraction snapshots are shown for two different values of the current. These results were obtained for the steel wire. As was mentioned above the key characteristics of the welding with the steel and ER5356 wires are qualitatively similar and we will be using in the discussion results obtained for both metals.

The model⁴ parameters in this simulations were the following: (i) scale of the Darcy force 10^8 ; (ii) scale of the additional frictional forces 5×10^5 ; (iii) viscosity triplet is $(10^6, 100, 0.001)$ [Pa.s]; (iv) electrical conductivity $(8\times10^7, 8\times10^6, 6\times10^6)$ [S/m]; (v) surface tension triplet (1.4;1.2;0.9); (vi) heat capacity and thermal conductivity are given in Fig. 11 (a) and (d).

^{4\}R56_L\ER5356\tun_test_I\out_E5356I120rcbd70g08Q1ga14_09et1e6_2_0001B3e5S8e7_ 8e6_6e6kp30F105_1e6Cp400vin13FD1e8_S

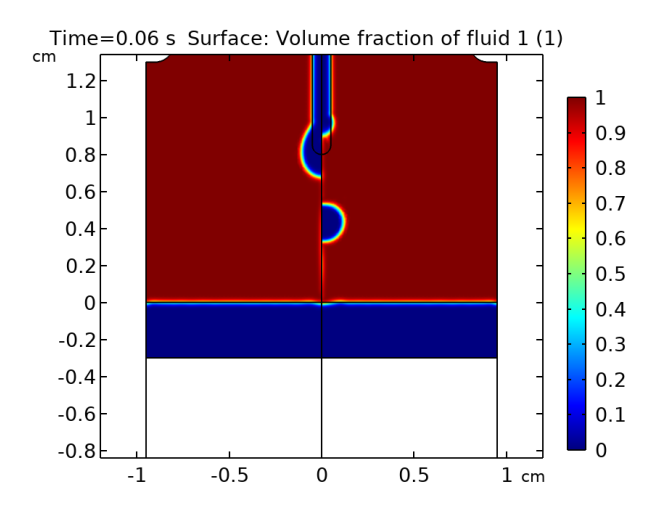


Figure 14. Current dependence of the volume fraction for two different values of the current: (left) I = 90 A; and (right) I = 120 A.

It can be seen from the figure that the transition from the spray to globular welding regime begins as the current is reduced from 120 A to 90 A. This behaviour is expected and correspond to experimental observations [34]. It was also shown that further increase of the current may result in the melting of the wire.

5.3 Effect of pressure

In this subsection we illustrate the effect of the pressure change on the welding regime in ER5356. The model⁵ parameters in these simulations were the following: (i) the Darcy force scale is 10^4 and additional frictional forces scale is 2×10^6 [N/m³]; (ii) viscosity triplet is (10^6 , 100, 0.001) [Pa.s]; (iii) electrical conductivity (8×10^7 , 8×10^6 , 6×10^6) [S/m]; (iv) surface tension triplet (1.4;1.2;0.9); (v) heat capacity and thermal conductivity are given in Fig. 11 (a) and (d).

The results of the simulations for three values of the pressure (1 atm, 0.5 atm, and 0.25 atm) are shown in Fig. 15. The results in each row are shown for two snapshots t = 0.0664 s (left) and t = 0.0774 s (right). The first row of the figure compares the volume fraction distribution obtained for P = 1 atm (left half) and P = 0.5 atm (right half). It can be seen from the figure that the main effect of the reduced pressure (from 1 to 0.5 atm) is an increase of the droplet frequency.

We note that further decrease of the Ar pressure from 0.5 to 0.25 atm has much smaller effect on the welding characteristics, see the 2-nd row in the Fig. 15. These are potentially important observations because of limited Argon supply on the ISS.

⁵\R56_L\ER5356\tun_P\out_E5356_I90wv_d70_g08_Q05_ga14_09_et1e6_2_0001_B3e5_S8e7_ 8e6_6e6_kp30_F11_1e6_Cp400_vin1_P05

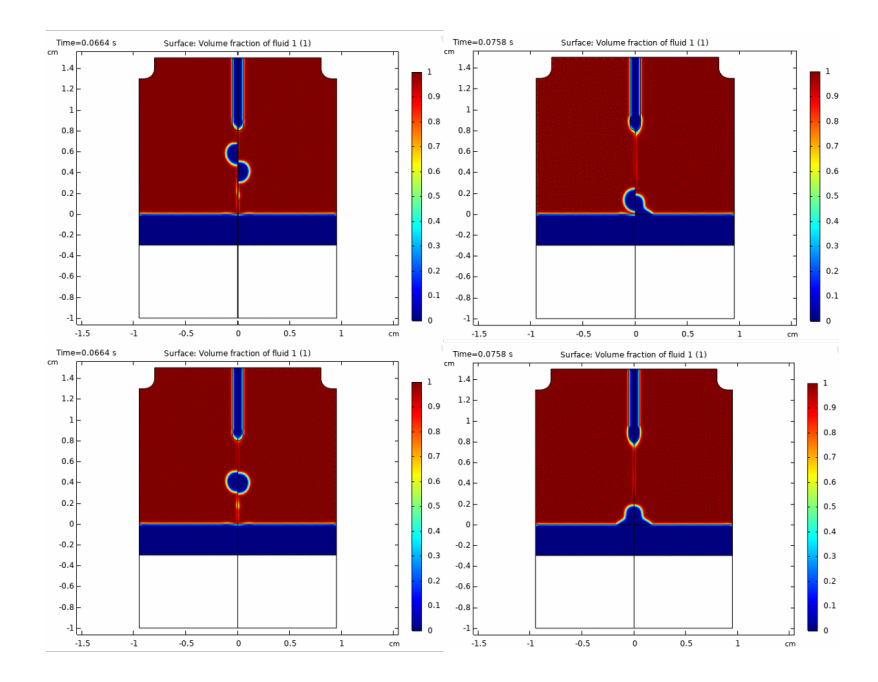


Figure 15. Pressure dependence of the volume fraction for three different values of the pressure: (i) P = 1 atm; (ii) P = 0.5 atm; and (iii) P = 0.25 atm. Each row compares results for two snapshots: 0.0664 s (left figure) and 0.0774 s (right figure). Top row shows snapshots for 1 atm left half with 0.5 atm right half for each figure. Bottom row compares snapshots for 0.5 atm left half with 0.25 atm right half for each figure.

5.4 Effect of gravity

Another important question is the dependence of the welding regime on gravity. This question is especially important in the context of the space applications and experiment on the ISS.

To estimate this effect we performed comparison of the welding characteristics for zero gravity with the results of the model performance on the ground for several sets of the model parameters. A typical result is shown in Fig. 16. In the figure a snapshot of the performance of the same model at time $t=0.0724~{\rm s}$ is shown for ground conditions (left half) and in zero gravity (right half).

The parameters of the model⁶ with the steel wire were the following (i) the Darcy force scale is 10^6 and additional frictional forces is 1×10^3 [N/m³]; (ii) viscosity triplet is (10^6 , 1000, 0.001) [Pa.s]; (iii) electrical conductivity (8×10^7 , 2×10^7 , 8×10^6) [S/m]; (iv) surface tension triplet (1.9;1.8;1.6); (v) heat capacity and thermal conductivity are given in the Fig. 3 (a) and (d).

It can be seen from the figure that the gravity effect is relatively small and leads to earlier separation of the droplet (small increase in droplet frequency). We note, that the obtained results are consistent with experimental observations [42]. The

⁶\R56_L\TUNING\TUNNING_gr\out_E_I200rec_d70g08Q1ga19_16et1e6_3_m3_B3e5S8e7_2e7_8e6kp0F105_1e3_G0

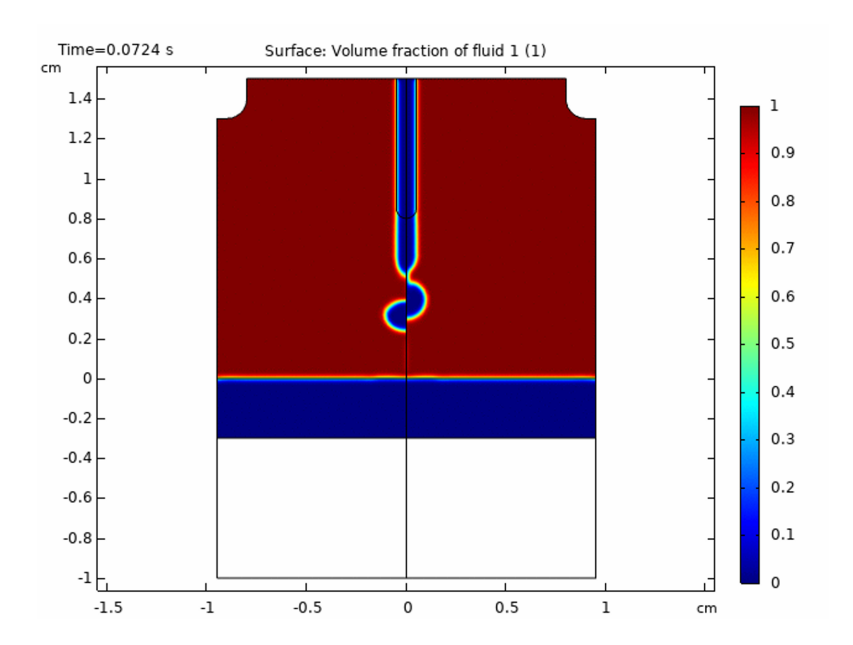


Figure 16. Snapshot of the droplet separation on the ground (left) and in zero-G condition (right).

latter observations show that gravity force is by an order of magnitude smaller as compared to the plasma force on the droplet.

Therefore, we conclude that the model predicts very moderate effect of the gravity on the welding dynamics. However, there is another important phenomenon closely related to the effect of gravity that may significantly effect the welding results in space. Namely, one may expect that zero gravity will effect the buoyancy effect.

5.5 Effect of buoyancy force

The buoyancy is important because it may strongly effect the quality of the weld. In the absence of the buoyancy the gas bubbles can be easily trapped in the melt pool. To study this phenomenon we have performed extensive simulations. Some results of the simulations are illustrated in Fig. 17. In this figure the snapshots of the meltpool are shown for two sets of parameters. In the first set (left half) there was no buoyancy force and the gas bubble trapped at the bottom of the meltpool can be seen in the figure. The parameters of the first set 7 with the steel wire were the following (i) the Darcy force scale is 10^6 [N/s/m 4] and additional frictional forces is zero; (ii) viscosity triplet is $(10^5, 1000, 0.001)$ [Pa.s]; (iii) electrical conductivity 8×10^5 [S/m]; (iv) surface tension 1.6; (v) heat capacity and thermal conductivity are given in the Fig. 3 (a) and (d).

For the second set the buoyancy force was added to the model and the bubble trapping effect was substantially reduced. The parameters of the second set ⁸ with

^{7\}R56_L\TUNING\D10\out_E75_I180_d022_g08_Q75_L1e4_HS4_eta_1e5_1e3_D10

^{8~\}TUNNING D6 buo\out E75 I160 d022 g08 Q6 L1e4 ga19 16 HS4 et1e6 1e5 B1

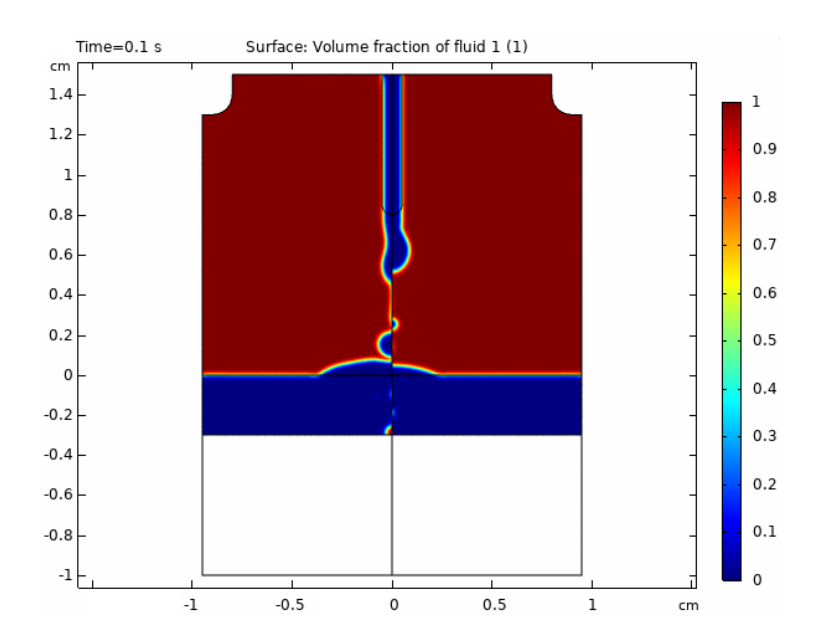


Figure 17. Snapshots of the droplet separation and meltpool formation without (left) and with (right) buoyancy force.

the steel wire were the following (i) the Darcy force scale is 10^6 [N/s/m⁴] and additional frictional forces is zero; (ii) viscosity triplet is (10^6 , 1000, 0.001) [Pa.s]; (iii) electrical conductivity triplet was (8×10^7 , 1×10^7 , 8×10^5), [S/m]; (iv) surface tension triplet (1.9;1.8; 1.6); (v) heat capacity and thermal conductivity are given in the Fig. 3 (a) and (d).

Based on our simulations we expect that buoyancy may significantly affect the meltpool strength. We note that the lack of buoyancy in space may be more essential for the zero-gravity application than the effect of gravity on the droplet transfer and detachment. The reason is that gravity in the region of ARC torch is screened by a very strong Lorentz force while buoyancy force in the mushy zone of the melt pool is dominating. We, therefore, expect that in space the strength of welded parts may be significantly affected by the discussed phenomenon.

5.6 Dependence on the specific heat

It was revealed in our simulations that specific heat capacity and its temperature dependence play a significant role in the dynamics and structure of the meltpool. Specifically, it is known from experiment and earlier simulations [12] that the melt pool in axisymmetric regime is growing at the average rate ≈ 2 mm/s and it responds like a gel to the droplet attachment. In this context it is interesting to note that the dynamics of the melt pool is strongly affected by the specific heat of metal.

An example of the simulation results for different values of the $C_p(T)$ is shown in Fig. 18. In the figure (a) the results for constant C_p are compared with those obtained for $C_p(T)$ given in Fig. 3 (a) but scaled as explained in the figure cap-

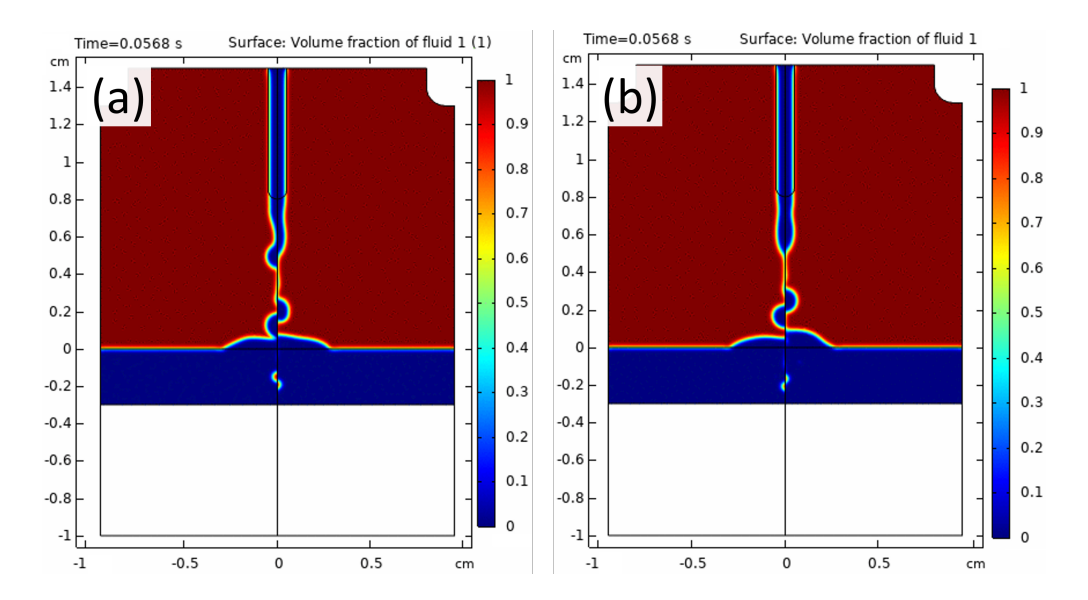


Figure 18. Snapshot of the droplet separation and transfer to the melt pool for steel wire. (a) Comparison of the two cases: (left half) specific heat given in Fig. 3 (a) scaled such that minimum value is 416 [J/kg/K] at 300 K and maximum value is 843 [J/kg/K] and (right half) constant specific heat ($C_p = 475$ [J/kg/K]). (b) Comparison of the two cases with specific heat given by Fig. 3 (a) and scaled such that: (left half) minimum and maximum values are the same as in the left half of figure (a) and (right half) minimum value is 216 [J/kg/K] and maximum value is 643 [J/kg/K].

tion. Other parameters of the model for this simulations 9 with steel wire were the following (i) the Darcy force scale is 10^6 [N/s/m 4] and additional frictional forces is zero; (ii) viscosity triplet is $(10^4, 10^4, 0.001)$ [Pa.s]; (iii) electrical conductivity 6×10^5 [S/m]; and (iv) surface tension 1.6.

It can be seen from the Fig. 18 (a) that substituting constant heat capacity with the temperature dependent value results in the change of the droplet frequency and slight change in the melt pool shape. Similar changes can be observed if one rescales the value of the $C_p(T)$ as explained in the figure caption for Fig. 18 (b). In particular, increasing the maximum value of the $C_p(T)$ leads to an increase of the frequency of the droplet detachment, increase of the width of the melt pool and decrease of the meltpool height. The latter observations are very important because heat capacity is one of the key parameters that enables control of the melt pool geometry. In addition, the temperature dependent heat capacity allows one to recover gel-like dynamical response of the melt pool to the droplet impingement in agreement with experimental observations.

We now consider another important parameter that controls the heat balance in the system, namely the heat conduction in the sheath layer.

 $^{^9\}R56_L\TUNING\TUNNING_Cp\out_E75_I180_d022_g08_Q10_L1e4_G16_S6e5_HS42_v1_D8_Cp475_kp30$

5.7 Dependence on the heat conduction in the sheath layer

We emphasise that there is a delicate balance of the heat sources and sinks that regulates the welding regime. One of the key parameters that control the heat balance is the heat source in the sheath layer Q_{int} , see discussion in Sec. 2.1.6. However, the issue of the whole approach based on magnetohydrodynamic approximation is that it breaks down in the sheath layer and there is no closed form self-consistent analytical or numerical method taking into account the heat transfer in this layer. An ad hoc correction of this problem was suggested in [12] and discussed in Sec. 2.1.6. It was suggested that such heat flux is proportional the maximum heat losses the ARC torch due to Joule effect. The coefficient K that scales this boundary heat source $Q_{int} \approx K \max \left(S_{JE} \right)$ is an important fitting parameter. Here we illustrate the dependence of the welding regime on this parameter.

In the Fig. 18 scaling factor K for Q_{int} has the value 10. We now compare the snapshots of the model dynamics with K equal 4 and 6 keeping all other parameters the same as in the previous section. The resulting snapshots are shown in Fig. 19.

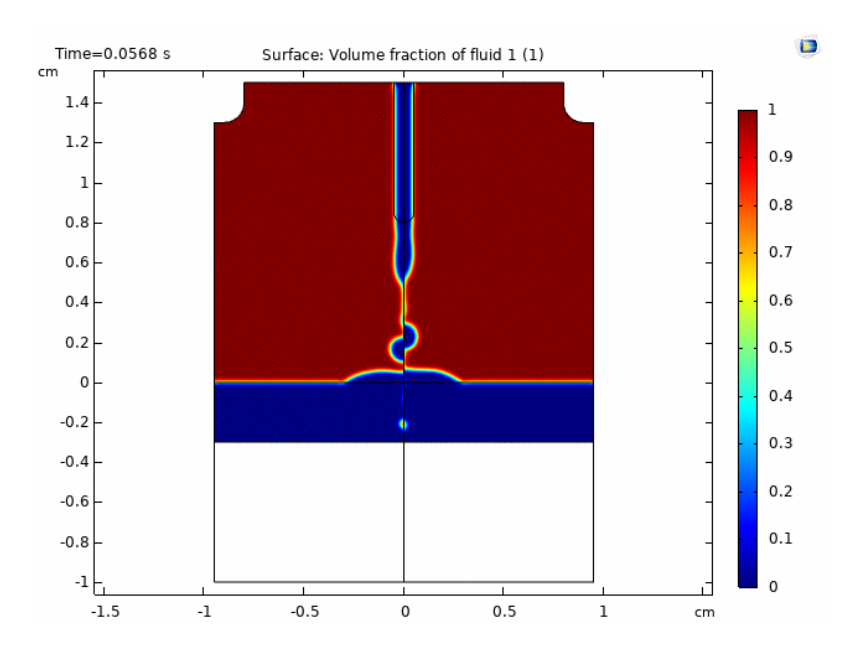


Figure 19. Snapshots of the droplet separation and transfer to the melt pool for steel wire and two values of the scaling coefficient K in the heat source Q_{int} . (left half) K = 6 and (right half) K = 4.

It can be seen from the figure that the changes induced by increasing the heat transfer in the sheath layer are similar to those observed due to changes in the heat capacity. Namely, changes of both parameters lead to increased droplet frequency and broadening the melt pool.

In addition, the heat transfer in the sheath layer controls the temperature of the droplet and melt pool surfaces. In particular, the reduced temperature of the droplets shown in Fig. 8 and 12 correspond to the reduced heat transfer rate in the

sheath layer. This is an important observation since it allows (to some extend) independent control of the frequency of the droplet detachment and its temperature as well as the temperature and dynamical response of the melt pool.

5.8 Spatter

There is another point of significant concern for space applications of the ARC welding. Namely, it is expected that the occurrence of the spatter may be harder to control and, therefore, it is potentially more dangerous in zero-G. An example of the spatter behaviour on the ground is shown in Fig. 20.

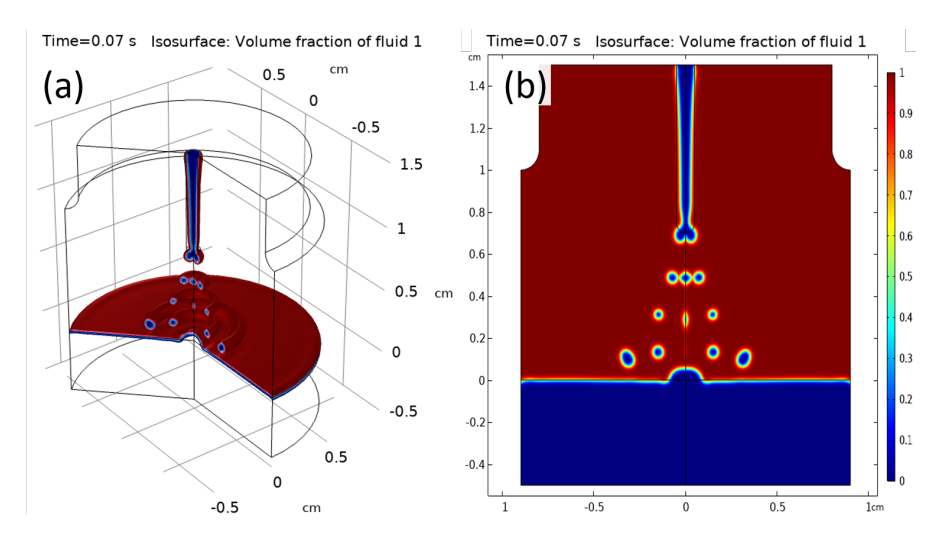


Figure 20. (a) 3D and (b) 2D view of the spatter pattern for the snapshot of welding simulations at time t=0.07~s.

Spatter behaviour on the ground is compared to the one in zero-G in Fig. 21. The parameters of this set¹⁰ with steel wire were the following (i) the Darcy force scale and additional frictional forces are zero; (ii) viscosity triplet is (100, 100, 0.001) [Pa.s]; (iii) electrical conductivity 4.032×10^7 [S/m]; (iv) surface tension 0.1; (v) heat capacity 475 [J/kg/K] and thermal conductivity 44.5 [W/m/K]. It can be seen from the figure that gravity significantly affects welding in the spatter case unlike in the nominal regime discussed earlier in the Sec. 5.4, see Fig. 16. This is because the melted wire in the region of the ARC torch is much more sensitive to the gravity than the solid wire.

A potential issue with the spatter in zero-G is an unbounded wondering of the hot sparks in the welding chamber. This problem can be further intensified by lowering the pressure in the chamber and this issue will be analysed in more details in the future work.

 $^{^{10}\ \}texttt{R56_L}\ \texttt{EMLM7_5}\ \texttt{SPATTER}\ \texttt{EMLM_7_vin1_I200_R_2c_a4_spatter}$

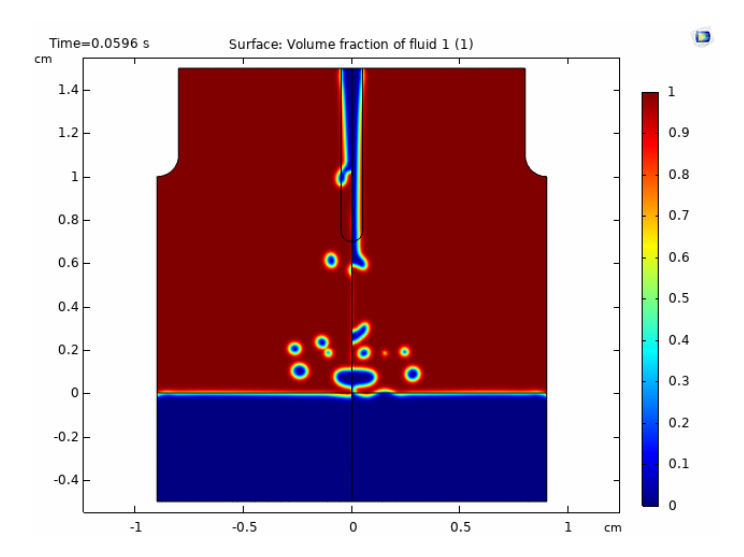


Figure 21. Comparison of the spatter dynamics in the presence of gravity (left) and in zero-G (b). The snapshot time t = 0.0596 s.

5.9 Evaporation

Our final example is the model based estimations of the metal evaporation rates. These estimations involve equation of the mass flux (26) and simulations of the temperature distribution in the wire, droplet and meltpool. The idea of the estimation is based on the fact that in the nominal welding regime the mass flow rate for both Al and iron has maximum at the boiling point and the temperature of the metal surfaces of the wire tip, droplet, and part of the meltpool should be close to the boiling point temperature.

We further note that the wire tip has radius of the same order of magnitude as the metal droplet. The area of the meltpool surface that can reach boiling point temperature can be estimated as the area of the spherical cap. The resulting estimate from above of the evaporation area is

$$A_{evap} = 4\pi r^2 \left(\frac{1}{2} + w\right) + 2\pi R_{mp} \cdot h_{mp}$$

where r is the radius of the droplet, R_{mp} is the radius of the meltpool; h is the height of the hot region of the meltpool, and w is the fraction of time required for the droplet transfer. Based on the results of simulations in this work and in the literature we assume the following values of the parameters for axisymmetric welding: (i) $r \approx 0.5$ mm for ER5356 and 0.7 mm for steel; (ii) $R_{mp} \approx 2.5$ -4 mm; (iii) $h_{mp} \approx 0.5$ -1 mm; and (iv) $w \approx 0.5$; area of the hot wire tip is half of the droplet area while w = 0.5.

Using equations for the maximum mass flux (see Sec. 2.2 eq. (26)) we obtain the following estimations for the mass flux: (i) 9 mgr/s/cm² for Al and (ii) 13 mgr/s/cm² for steel (iron). The resulting evaporation rate is: (i) 0.23 [gr/min] for Al and (ii) 0.57 [gr/min] for steel. The main difference comes from the fact that the steel evaporation area is larger because its wire diameter is larger while mass fluxes

have similar values for both metals. We note that the results of estimations strongly depend on the wire geometry and other parameters of the system and should only be considered as ballpark estimations. More accurate estimations require model validation and will be performed in the future work.

6 Conclusions

To summarise, we developed 2D axisymmetric finite element model of the ARC welding using COMSOL Multiphysics. This model is used to support experimental welding work on the ISS. Two versions of the model were developed: (i) stationary axisymmetric model of the ARC torch and (ii) dynamical axisymmetric model of droplet detachment and transfer. The model is using magnetohydrodynamics approximation of the flow in the ARC torch and includes the following physics: (i) level set approximation of the two-phase (liquid metal/Ar gas) flow; (ii) laminar two-phase flow equations for the mass, momentum, and energy conservation; (iii) nonisothermal heat transfer; (iv) electric currents; and (v) and magnetic fields. The nonisothermal heat transfer involves multiple heat sources including: (i) electron heating of the anode wire; (ii) ion heating and electron cooling of the substrate; (iii) radiative cooling of the metal surface and Ar bulk flow; and (iv) additional heat source in the sheath layer at the wire tip/plasma interface. The model takes into account many important force including gravity and Lorentz forces, Darcy force, surface tension, and additional frictional force.

Stationary model includes temperature dependent thermophysical parameters of Ar flow such as density, electrical and thermal conductivity, heat capacity, viscosity, and net emission coefficient. The metal parameters of this model were constant. It was shown that the stationary model can reasonably well reproduce the temperature distribution in the ARC torch. The model allows to analyse effect of many system parameters on the ARC torch including e.g. (i) current; (ii) Ar flow rate; (iii) model geometry; (iv) density; (v) thermal and electrical conductivities of the wire material etc. An example of the parametric studies of the convective heat transfer in the ARC torch as a function of the Ar inlet flow rate is shown in Sec. 3.1. In particular, this example demonstrates the importance of the convective heat transfer for the temperature distribution in the torch, strong dependence of the heat transfer on the inlet velocity, and existence of the optimal velocity for the maximum heat transfer in plasma below the wire tip.

Dynamical axisymmetric model of the droplet detachment, transfer, and the meltpool build up includes temperature dependent thermophysical properties of the gas flow, metal wire, and metal substrate. The model has been developed for steel wire and then extended to include ER5356 alloy wire. It was shown that the model can reasonably well reproduce the shape and frequency of the droplet detachment and initial shaping and dynamical response of the melt pool. We note that the temperature dependence of many thermophysical parameters is not well known. This is especially important for alloy ER5356 where temperature dependence for most parameters is known only approximately and locally. Further analysis and validation will be required in the future work to improve accuracy of

the model predictions. At present model provides deep physical insight into the system dynamics and allows for semi-quantitative predictions of various welding regimes.

In this report we highlighted some of the model applications to the analysis of welding regimes. In particular, we reported dependence of the welding regime on the current in Sec. 5.2. It was shown that the current increase results in transition from the globular to spray regime in agreement with earlier experimental observations. Next, it was shown (Sec. 5.8) that further increase of the current may result in melting the wire and spatter. The spatter is important in the context of space applications because of unbounded wondering of sparks in the welding chamber.

At the same time we did not observe a significant effect of the zero-gravity environment on the nominal welding regime, see Sec. 5.4, except of small increase in the droplet frequency and volume in zero-G. It was noted that in the region of the ARC torch the gravity force is relatively small as compared to the Lorentz force.

It was also noted that reducing chamber pressure to half atmosphere does not significantly affect the nominal welding regime 5.3 in simulations. This observation is important for the ISS experiments because of limited supply of Ar.

At the same time an important observation, see Sec. 5.5 was that in zero-G environment the quality of the melt may be deteriorated because of the lack of the buoyancy effect and subsequent trapping of the gas bubbles in the melt.

It was further noticed in Sec. 5.6 that specific heat capacity and its temperature dependence are important thermophysical parameters of the model that allow one to control shape of the meltpool and its dynamical response to the droplet impingement. Another important parameter highlighted in the report, see Sec. 5.7, was the heat transfer from the wire tip to plasma that controls droplet frequency and shape as well as the temperature of the ARC and meltpool.

In our last example, see Sec. 5.9 we used results of simulations to estimate from the above the rates of metal evaporation for both steel and ER5356 wires. The resulting rates are 0.23 [gr/min] for ER5356 and 0.57 [gr/min] for the steel.

Finally, we note that the developed model can be used to understand physics of the ARC welding in various environments and different geometries. Specifically, the model analysis in zero gravity reveals that there is significant increase in probability of gas bubbles trapping in the meltpool in the absence of Buoyancy effect. In addition, there is a possibility of unbounded wondering of sparks in the welding chamber in zero gravity. These phenomena raise concern of quality of the weld and safety for ISS applications. Also metal evaporation in the confined ISS environment should be further considered in more details especially for the case of spatter, when the evaporation area may be significantly increased.

Future work will include validation of the results using available experimental data and extension 2D axisymmetric model to 3D model.

References

- 1. D. Tamir, Thomas A. Siewert, Koichi Matsubuchi, Flanigan Lee, Renjeng Su, and Thomas W. Eagar. In-space welding visions&realities. In *Proceedings of the Thirtieth Space Congress Yesterday's Vision is Tomorrow's Reality*, pages 1–8, 1993.
- 2. N. Naden and P.J. Prater. A review of welding in space. *NASA/TM-2020-220557*, 2020.
- 3. American Welding Society. Welding in space. https://awo.aws.org/2015/07/welding-in-space/, 2015.
- 4. H G Fan and R Kovacevic. A unified model of transport phenomena in gas metal arc welding including electrode, arc plasma and molten pool. *Journal of Physics D: Applied Physics*, 37(18):2531–2544, sep 2004.
- 5. F Lago, J J Gonzalez, P Freton, and A Gleizes. A numerical modelling of an electric arc and its interaction with the anode: Part i. the two-dimensional model. *Journal of Physics D: Applied Physics*, 37(6):883–897, feb 2004.
- 6. M Tanaka. An introduction to physical phenomena in arc welding processes. *Welding International*, 18(11):845–851, nov 2004.
- 7. A. Traidia and F. Roger. Numerical and experimental study of arc and weld pool behaviour for pulsed current GTA welding. *International Journal of Heat and Mass Transfer*, 54(9-10):2163–2179, apr 2011.
- 8. M Hertel, A Spille-Kohoff, U Füssel, and M Schnick. Numerical simulation of droplet detachment in pulsed gas—metal arc welding including the influence of metal vapour. *Journal of Physics D: Applied Physics*, 46(22):224003, may 2013.
- 9. Linmin Li, Baokuan Li, Lichao Liu, and Yuichi Motoyama. Numerical modeling of fluid flow, heat transfer and arc-melt interaction in tungsten inert gas welding. *High Temperature Materials and Processes*, 36(4):427–439, apr 2017.
- 10. Cadiou, Stephen, Courtois, Mickaël, Carin, Muriel, Le Masson, Philippe, Guilmois, Lauriane, and Paillard, Pascal. Development of a two-dimensional axial symmetry model for wire arc additive manufacturing. In *Mathematical Modelling Of Weld Phenomena* 12. Verlag der Technischen Universität Graz, 2018.
- 11. S. Cadiou, M. Courtois, M. Carin, W. Berckmans, and P. Le masson. 3d heat transfer, fluid flow and electromagnetic model for cold metal transfer wire arc additive manufacturing (cmt-waam). *Additive Manufacturing*, 36:101541, dec 2020.
- 12. S. Cadiou, M. Courtois, M. Carin, W. Berckmans, and P. Le Masson. Heat transfer, fluid flow and electromagnetic model of droplets generation and melt pool behaviour for wire arc additive manufacturing. *International Journal of Heat and Mass Transfer*, 148:119102, feb 2020.

- 13. Michael R. Zachariah and Michael J. Carrier. Molecular dynamics computation of gas-phase nanoparticle sintering: a comparison with phenomenological models. *Journal of Aerosol Science*, 30(9):1139–1151, oct 1999.
- 14. COMSOL. Comsol multiphysics reference manual, version 5.5, comsol inc., 2020.
- 15. Yosuke Ogino and Yoshinori Hirata. Numerical simulation of metal transfer in argon gas-shielded GMAW. *Welding in the World*, 59(4):465–473, jan 2015.
- 16. J J Lowke, R Morrow, and J Haidar. A simplified unified theory of arcs and their electrodes. *Journal of Physics D: Applied Physics*, 30(14):2033–2042, jul 1997.
- 17. Marco A Ramirez, Gerardo Trapaga, and John McKelliget. A comparison between two different numerical formulations of welding arc simulation. *Modelling and Simulation in Materials Science and Engineering*, 11(4):675–695, jun 2003.
- 18. Stanley Osher and James A Sethian. Fronts propagating with curvature-dependent speed: Algorithms based on hamilton-jacobi formulations. *Journal of Computational Physics*, 79(1):12–49, nov 1988.
- 19. Joongkil Choe, Han Gyeol Kim, Youngjin Jeon, Hyeok Jun Park, Youngjo Kang, Shumpei Ozawa, and Joonho Lee. Surface tension measurements of 430 stainless steel. *ISIJ International*, 54(9):2104–2108, 2014.
- 20. Yangyang Zhao, Phill-Seung Lee, and Hyun Chung. Effect of pulsing parameters on drop transfer dynamics and heat transfer behavior in pulsed gas metal arc welding. *International Journal of Heat and Mass Transfer*, 129:1110–1122, feb 2019.
- 21. Kamlesh Mundra. Toward understanding alloying element vaporization during laser beam welding of stainless steel. *Welding Journal*, 72, 1993.
- 22. Alexander Klassen, Vera E. Forster, Vera Juechter, and Carolin Körner. Numerical simulation of multi-component evaporation during selective electron beam melting of TiAl. *Journal of Materials Processing Technology*, 247:280–288, sep 2017.
- 23. Alexander Klassen, Thorsten Scharowsky, and Carolin Körner. Evaporation model for beam based additive manufacturing using free surface lattice boltzmann methods. *Journal of Physics D: Applied Physics*, 47(27):275303, jun 2014.
- 24. David Lide. *CRC handbook of chemistry and physics : a ready-reference book of chemical and physical data.* CRC Press, online version. Boca Raton, Fla, 84th, section 4, properties of the elements and inorganic compounds; vapor pressure of the metallic elements edition, 2003.

- 25. Wikipedia. Vapor pressures of the elements (data page) Wikipedia, the free encyclopedia. http://en.wikipedia.org/w/index.php?title=Vapor%20pressures%20of%20the%20elements%20(data%20page)&oldid=1025693823, 2021. [Online; accessed 28-September-2021].
- 26. online. Heat of vaporization. https://gchem.cm.utexas.edu/data/section2.php?target=heat-transition.php.
- 27. Y. Ogino, Y. Hirata, and S. Asai. Numerical simulation of metal transfer in pulsed-MIG welding. *Welding in the World*, 61(6):1289–1296, jun 2017.
- 28. R. T. C. Choo, J. Szekely, and R. C. Westhoff. On the calculation of the free surface temperature of gas-tungsten-arc weld pools from first principles: Part i. modeling the welding arc. *Metallurgical and Materials Transactions B*, 23(3):357–369, jun 1992.
- 29. Shanping Lu, Hidetoshi Fujii, and Kiyoshi Nogi. Marangoni convection and weld shape variations in ar–o2 and ar–CO2 shielded GTA welding. *Materials Science and Engineering: A*, 380(1-2):290–297, aug 2004.
- 30. C S Kim. Thermophysical properties of stainless steels. Technical report, Argonne National Lab., Ill. (USA), sep 1975.
- 31. Engineering Toolbox. Stainless steel aisi 310 properties. https://www.engineeringtoolbox.com/stainless-steel-310-properties-d_2167.html, 2019.
- 32. Vladimir V. Mirkovich, editor. *Thermal Conductivity and Electrical Resistivity of Eight Selected AISI Stainless Steels*, pages 79–104. Springer US, Boston, MA, 1978.
- 33. M. I. Boulos, P. Fauchais, and Emil Pfender. *Thermal Plasmas*. Springer US, June 2013.
- 34. Yangyang Zhao and Hyun Chung. Numerical simulation of the transition of metal transfer from globular to spray mode in gas metal arc welding using phase field method. *Journal of Materials Processing Technology*, 251:251–261, jan 2018.
- 35. H.G. Fan, H.L. Tsai, and S.J. Na. Heat transfer and fluid flow in a partially or fully penetrated weld pool in gas tungsten arc welding. *International Journal of Heat and Mass Transfer*, 44(2):417–428, aug 2001.
- 36. Manabu Tanaka, Hidenori Terasaki, Masao Ushio, and John J. Lowke. A unified numerical modeling of stationary tungsten-inert-gas welding process. *Metallurgical and Materials Transactions A*, 33(7):2043–2052, jul 2002.
- 37. K. C. Hsu, K. Etemadi, and E. Pfender. Study of the free-burning high-intensity argon arc. *Journal of Applied Physics*, 54(3):1293–1301, mar 1983.

- 38. J. Hu and H.L. Tsai. Heat and mass transfer in gas metal arc welding. part i: The arc. *International Journal of Heat and Mass Transfer*, 50(5-6):833–846, mar 2007.
- 39. Xiangman Zhou, Haiou Zhang, Guilan Wang, and Xingwang Bai. Three-dimensional numerical simulation of arc and metal transport in arc welding based additive manufacturing. *International Journal of Heat and Mass Transfer*, 103:521–537, dec 2016.
- 40. Dae-Won Cho, Jin-Hyeong Park, and Hyeong-Soon Moon. A study on molten pool behavior in the one pulse one drop GMAW process using computational fluid dynamics. *International Journal of Heat and Mass Transfer*, 139:848–859, aug 2019.
- 41. Kei Yamazaki, Eri Yamamoto, Keiichi Suzuki, Fusaki Koshiishi, Kenji Waki, Shinichi Tashiro, Manabu Tanaka, and Kazuhiro Nakata. The measurement of metal droplet temperature in GMA welding by infrared two-colour pyrometry. *Welding International*, 24(2):81–87, feb 2010.
- 42. Ke Li, Zhisheng Wu, and Cuirong Liu. Measurement and calculation of plasma drag force in arc welding based on high-speed photography technology and particle dynamics. 85:97–101, nov 2015.
- 43. Ivaldo Leão Ferreira, José Adilson de Castro, and Amauri Garcia. Dependence of surface tension and viscosity on temperature in multicomponent alloys. In *Wettability and Interfacial Phenomena Implications for Material Processing*. IntechOpen, may 2019.

REPORT DOCUMENTATION PAGE

2. REPORT TYPE

1. REPORT DATE (DD-MM-YYYY)

Form Approved OMB No. 0704-0188

3. DATES COVERED (From - To)

The public reporting burden for this collection of information is estimated to average 1 hour per response, including the time for reviewing instructions, searching existing data sources, gathering and maintaining the data needed, and completing and reviewing the collection of information. Send comments regarding this burden estimate or any other aspect of this collection of information, including suggestions for reducing this burden, to Department of Defense, Washington Headquarters Services, Directorate for Information Operations and Reports (0704-0188), 1215 Jefferson Davis Highway, Suite 1204, Arlington, Wa 22202-4302. Respondents should be aware that notwithstanding any other provision of law, no person shall be subject to any penalty for failing to comply with a collection of information if it does not display a currently valid OMB control number.

PLEASE DO NOT RETURN YOUR FORM TO THE ABOVE ADDRESS.

| 01-10-2021 | | Techni | cal Memorandum | | | 10/2020-09/2021 |
|-----------------------------|--|---------------------------------------|--------------------------|---------------|-----------|---|
| 4. TITLE AND SU | JBTITLE | <u> </u> | | | 5a. CON | TRACT NUMBER |
| Analysis of a | rc welding pro | ocess in space | | | | |
| | | | | | 5h GRA | NT NUMBER |
| | | | | | Job. Gill | INT NOMBER |
| | | | | | | |
| | | | | | 5c. PRO | GRAM ELEMENT NUMBER |
| | | | | | | |
| 6. AUTHOR(S) | | | | | 5d. PRO | JECT NUMBER |
| Dmitry G. Lu | ichinsky, Vasy | l Hafiychuk, K | evin R. Wheeler, Chris | topher E. | | |
| Roberts, Ian | | • | | 1 | Fo. TACI | KNUMBER |
| | | | | | | .03.00.004.001 |
| | | | | | 13102 | .03.00.004.001 |
| | | | | | 5f. WOR | K UNIT NUMBER |
| | | | | | | |
| 7 DEDECRING | 0004111747101 | INAME(O) AND A | DDDE00/F0\ | | | Lo DEDECRINO ODGANIZATION |
| | Research Cent | NAME(S) AND A | DDRESS(ES) | | | 8. PERFORMING ORGANIZATION REPORT NUMBER |
| | , California 94 | | | | | L-12456 |
| ivionett i ieiu | , cumomia > 1 | 2177 | | | | |
| | | | | | | |
| | | | AND ADDRESS (50) | | | |
| | | | AND ADDRESS(ES) | | | 10. SPONSOR/MONITOR'S ACRONYM(S) NASA |
| | | Space Adminis | tration | | | INASA |
| wasnington, | DC 20546-000 | 01 | | | | 11. SPONSOR/MONITOR'S REPORT |
| | | | | | | NUMBER(S) |
| | | | | | | NASA/TM-2021-0022016 |
| 12 DISTRIBUTIO | ON/AVAILABILITY | STATEMENT | | | | |
| Unclassified- | | · · · · · · · · · · · · · · · · · · · | | | | |
| Subject Cates | | | | | | |
| | | gram (757) 86 | 4-9658 | | | |
| 13. SUPPLEMEN | | <u> </u> | | | | |
| An electronic v | ersion can be fo | ound at http://ntr | s.nasa.gov. | | | |
| | | | - | | | |
| 14. ABSTRACT | | | | | | |
| | | | | | | is expected that deployment of welding |
| | | | | | | to revolutionise how orbiting platforms are |
| | | | | | | uality of a weld is extremely dependent on |
| | | | | | | be tough to manage as gases behave |
| | | | | | | related to the spatter and sparks dynamics |
| | | | | | | ses by computational modelling. To |
| | | | | | | etachment and transfer, and the melt pool |
| | | | | | | phase liquid metal/gas flow modelling. |
| Two finite ele | ement models | were built usi | ng 2D axisymmetric ge | cometry in CO | OMSOL I | Multiphysics [®] : (i) stationary model of the |
| 15. SUBJECT TE | rd (ii) dynamic | cal model of di | roplet detachment and | transter. Bol | th model | s demonstrate reasonable agreement with |
| ARC welding | earlier experimental observations and high sensitivity to the temperature dependence of the thermophysical parameters on the ARC welding, metals, in space manufacturing, finite element modelling system materials. The models were used to provide physical insight into ARC welding in various environments and geometries. | | | | | |
| It was shown | in particular | that there is a | io provide physical ilis | agni mio Aki | loc trans | ping in the meltpool and a possibility of |
| | - | | - | - | | |
| | | | | | | nevor hespensible personoration rate that of quality of the weld and safety for JSS |
| a: REPORT and applications. | D. ABSTRACT | c. THIS PAGE | | PAGES | | · · · · · · · · · · · · · · · · · · · |
| U | U | U | UU | 27 | | EPHONE NUMBER (Include area code) |
| ٥ | | | | 37 | (757) 8 | 64-9658 |